



## PRICING AUTOCALLABLES UNDER LOCAL-STOCHASTIC VOLATILITY

WALTER FARKAS<sup>✉1,3,4</sup>, FRANCESCO FERRARI<sup>✉1</sup> AND URBAN ULRYCH<sup>✉1,2,4</sup>

<sup>1</sup>Department of Banking and Finance, University of Zurich, Switzerland

<sup>2</sup>College of Management of Technology, EPFL Lausanne, Switzerland

<sup>3</sup>Department of Mathematics, ETH Zurich, Switzerland

<sup>4</sup>Swiss Finance Institute, Switzerland

(Communicated by Robert Jarrow and Dilip Madan)

**ABSTRACT.** This paper investigates the pricing of single-asset autocallable barrier reverse convertibles in the Heston local-stochastic volatility (LSV) model. Despite their complexity, autocallable structured notes are the most traded equity-linked exotic derivatives. The autocallable payoff embeds an early-redemption feature generating strong path- and model-dependency. Consequently, the commonly-used local volatility (LV) model is overly simplified for pricing and risk management. Given its ability to match the implied volatility smile and reproduce its realistic dynamics, the LSV model is, in contrast, better suited for exotic derivatives such as autocallables. We use quasi-Monte Carlo methods to study the pricing given the Heston LSV model and compare it with the LV model. In particular, we establish the sensitivity of the valuation differences of autocallables between the two models with respect to payoff features, model parameters, underlying characteristics, and volatility regimes. We find that the improved spot-volatility dynamics captured by the Heston LSV model typically result in higher prices, demonstrating the dependence of autocallables on the forward-skew and vol-of-vol risk. Moreover, we show that the parameters of the stochastic component of LSV models enable controlling for the autocallables price while leaving the fit to European options unaffected.

**1. Introduction.** Equity-linked yield enhancement structured notes offer more attractive returns compared to traditional fixed-income securities. Accordingly, such exotic derivatives experience great demand, especially in low-interest rate environments. Structured notes are unsecured debt obligations comprising a bond and typically a single or multiple derivative payoffs. The barrier reverse convertible (BRC) is one such yield enhancement structured product. It consists of a zero-coupon bond, a short down-and-in (D&I) put option, and a stream of coupon payments. The autocall feature complements the BRC with Bermudan up-and-out (U&O) barriers, which, if hit, trigger the early redemption of the note. As a result of the increased risk exposure, autocallables offer higher coupons compared to standard

2020 *Mathematics Subject Classification.* Primary: 91G20, 91G60; Secondary: 62P05.

*Key words and phrases.* Exotic derivatives pricing, local-stochastic volatility, implied volatility smile dynamics, autocallables, barrier reverse convertibles, quasi-Monte Carlo methods.

\*Corresponding author: Walter Farkas.

fixed maturity structured products. Therefore, they can provide a better fit to the risk-return appetite of investors who are seeking income in low-yield environments.

The issuance volume of such exotic derivatives has increased exponentially since the first autocallable was traded in 2003 [12]. According to [40], autocallable products are the most traded equity-linked exotic derivatives of the last 20 years, with average yearly volumes topping 100 billion euros. Despite their high demand, the hedging of such derivatives continues to be problematic due to their significant path-dependency and complex dynamics [42]. Furthermore, leading issuers have recently experienced trading losses, forcing them to rethink this business [4, 5].

The local volatility (LV) model, first proposed in [15] and [13] as an extension of the Black-Scholes model [7] capable of reproducing the observed implied volatility (IV) smile, remains to date a standard model for pricing and risk managing structured derivatives at equity trading desks [11, 44]. However, its limitations are widely documented in the literature. In particular, the LV model does not capture the realistic dynamics of the IV smile [14, 26, 38] and thus systematically misprices the forward-smile and the vol-of-vol risk [6]. Autocallables are sensitive to the IV dynamics because of their path-dependent nature. Consequently, the LV model is in general not suited for pricing and hedging autocallables [11].

Stochastic volatility (SV) models, such as the Heston model [30], tend to be more consistent with the observed market dynamics but are commonly not able to fit the short-end of the implied volatility surface (IVS). The local-stochastic volatility model, introduced by [32], aims to address the limitations of LV and SV models by combining their advantages. Hence, the local-stochastic volatility (LSV) model is consistent with the market prices of European options and the dynamics of the IV smile. As such, it oughts to be suitable for modeling exotic options such as those embedded in autocallable derivatives.

Despite the popularity of autocallables, the academic literature has dedicated limited attention to them [23]. From a qualitative viewpoint, [8] present several autocallable payoffs and discuss the embedded risks as well as the hedging implications. The references to valuation methods include a partial differential equation (PDE) framework for autocallables with discrete and continuous U&O barriers [12], an analytical pricing formula in a Black-Scholes setting [23], an LV valuation add-on accounting for the complex spot-volatility dynamics [40], and a recursive method to obtain a static hedging portfolio replicating the payoff under a general Markov diffusion [34].

On the other hand, employing Monte Carlo (MC) methods, [18] suggest a specific variance reduction technique for pricing autocallables, and [2] develop an algorithm that allows for stable differentiation to improve the calculation of Greeks. The autocallables literature in an LSV setting contains an analysis of the impact of SV in the case of a multi-asset autocallable referencing the worst performing underlying in a basket [11]. Moreover, a brief comparison of an FX autocallable price under LV versus LSV is given in [10] within the context of a study of the convergence of an Euler scheme for a Heston-like LSV model.

The impact of boosting LV with an SV component may be well understood by practitioners for a single-asset autocallable [11], yet, to the best of our knowledge, no academic paper provides an extensive analysis of its prices in LV versus LSV models. In light of the industry relevance, the central purpose of this paper is to perform such analysis. In the existing LSV literature, such comparison is done, e.g., on forward-starting options in [44]. [32], [9], and [43] present some results

for American-style binary and barrier FX options in the Heston LSV model. [29] and [41] study the price difference of call spread cliques. Finally, [39] exhibit a price comparison of at-the-money (ATM) straddles on the realized variance and the VIX index.

In this paper, we compare the fair values of different single-asset autocallable BRCs referencing major US indices obtained with the LSV and the LV models. In the spirit of [32], we augment the LV model with the Heston SV model [30]. Therefore, the LSV model resulting from matching the diffusion terms of both models using Gyöngy's mimicking theorem [25] is Heston-like. We calibrate the LSV model with the non-parametric Monte Carlo (MC) approach of [44]. The LV function is obtained through its association to the IVS via the Dupire's formula, whereby the extended surface stochastic volatility inspired (eSSVI) parametrization [28] is employed to obtain a smooth arbitrage-free IVS.

We aim to identify the autocallables payoff features that embed the largest model-dependency, study the sensitivity of the callable price with respect to the Heston parameters, and the impact of underlying specific characteristics as well as the evolution of valuation differences with the volatility regime. The price estimates are obtained with quasi-MC (QMC) methods and antithetic variates for variance reduction. Generally, we find callable derivatives to be valued higher in the Heston LSV model compared to the LV model, and hence the price differences to be positive. In particular, our analysis consists of four parts.

First, we study the impact of payoff features and identify those that imply larger price differences between the LSV and LV models. Namely, the features embedding higher model-dependency as well as exposure to the vol-of-vol and the forward-smile risk. Indeed, we establish that the composition of the callable payoff has an impact on the valuation differences. For instance, longer U&O barrier observation tenors and higher coupon levels lead to larger price differences, whereas the effect of higher D&I barrier levels is decreasing or increasing depending on the maturity of the note.

Second, we test the effect of changing the parameters driving the stochastic component of the Heston LSV model. The observed impact is reduced to the SV parameters as the prices of European options are unchanged by construction. The valuation differences increase with the volatility-of-variance  $\eta$ , whereas they decrease with the speed of mean reversion  $\kappa$ , the correlation  $\rho$ , and the long-term level of variance  $\theta$ . The effect of the initial level of variance  $V_0$  is negligible. We motivate our observation based on the respective resulting forward IV skews.

Third, we analyze underlying specific characteristics such as the dividend yield and the implied volatility level. We find that lower forwards reduce the valuation differences. Indeed, for sufficiently low forward and long maturity, the Heston LSV price becomes even smaller than the LV price. Moreover, underlyings exhibiting higher implied volatility levels tend to produce larger valuation differences.

Finally, we study the impact of the volatility regime. We find the difference between Heston LSV and LV model valuations to be positively related to the market's implied volatility level. This is only partially explained by higher coupons that can be financed by selling a more expensive put option. Indeed, the main drivers are the higher volatility-of-variance  $\eta$  and lower spot-variance correlation  $\rho$  resulting from the calibration of the Heston model in stressed markets.

The paper is organized as follows. Section 2 presents the employed dataset and the construction of an arbitrage-free IVS, which serves as the foundation of the paper. Section 3 defines the LSV model and discusses its advantages in comparison to the LV and SV models. Section 4 studies the impact of payoff features, model parameters, underlying characteristics, and market regimes on the autocallable price difference in the Heston LSV and LV models. Section 5 concludes. Additional explanations and figures are delegated to Appendices A and B.

## 2. Implied volatility surface.

**2.1. Dataset.** The dataset employed in our analysis is retrieved from IvyDB US, which is a comprehensive database of historical prices for the entire US listed index and equity options markets compiled by OptionMetrics and accessible through the Wharton Research Data Services [36]. We obtain US dollar zero-coupon interest rate curves, underlying security prices, and the corresponding historical option prices.

The historical option price data contains the best bid and offer prices across all exchanges. In accordance with the standard market convention, we use mid option prices to compute implied forwards, implied dividend yields inclusive of borrow rates, and implied volatilities. To ensure that we retain only informative options, we filter the dataset as follows: we drop in-the-money (ITM) options because they are notably inaccurate due to infrequent trading, and we exclude options with bid prices under twice the minimum tick size of USD 0.05, i.e., USD 0.10 [1]. Moreover, for expiries where both A.M. and P.M. settled options are listed, we drop options with P.M. settlement from the dataset.

In our experiments, we focus on US broad equity market indices such as the S&P 500 (SPX), the Nasdaq-100 (NDX), the Dow Jones Industrial Average (DJX), and the Russell 2000 (RUT). First, excluding a few exceptions, index options are European style in contrast to American style stock options. Hence, we can readily use Black-Scholes (BS) formula to price these options and compute implied volatilities. Second, by focusing on equity indices, we avoid the non-trivial treatment of discrete cash dividends coupled with proportional dividends and their prediction. Third, the liquidity of index options is notably higher than their single stock equivalents, and additionally, more listed expiries are available. Therefore, greater and more reliable data points can be used as inputs in the calibration of the model and the implied volatility surface parametrization. Fourth, autocallable structured notes referencing US equity indices represent a large share of the equity exotic derivatives market. These arguments justify our choice.

**2.2. Parametrization.** When pricing exotic path-dependent derivatives in accordance with market observed vanilla option prices, the implied volatility surface serves as the crucial input parameter of any pricing model. The absence of static arbitrage is key. In fact, any arbitrage violation can lead to mispricings occurring due to negative transition probabilities [16].

For the Black-Scholes option price  $C^{BS}(\cdot)$  and the market observed option price  $C^{MKT}(\cdot)$ , both referencing the same underlying, implied volatility is defined as the value  $\hat{\sigma}$  such that  $C^{BS}(K, T, \hat{\sigma}) = C^{MKT}(K, T)$ . Namely, it is the value of the volatility parameter  $\sigma$  that matches the observed market price with the price obtained using the Black-Scholes formula. Implied volatilities generally form a U-shaped pattern across strikes. Consequently, the function  $K \mapsto \hat{\sigma}(K, T)$ , which, for any fixed maturity  $T$ , assigns to each strike  $K$  the value  $\hat{\sigma}(K, T)$ , is commonly

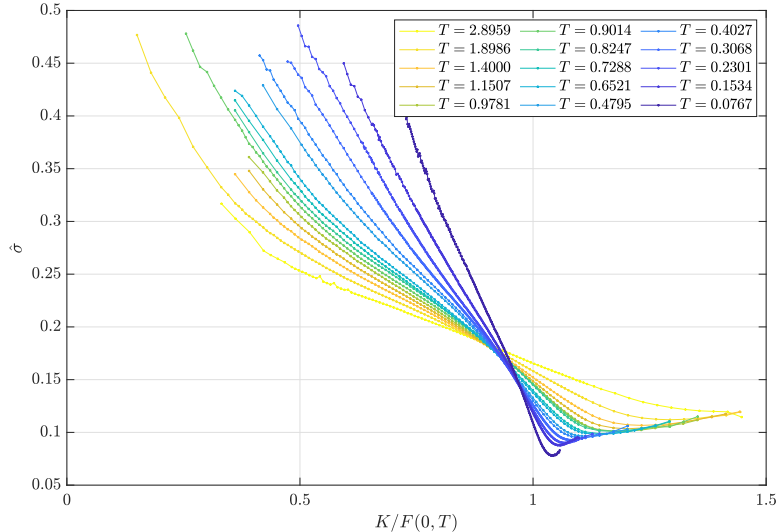


FIGURE 1. Implied volatilities in forward-moneyness  $K/F(0, T)$  space computed from SPX mid option prices across all the listed regular expiries as of January 23, 2020.

referred to as the IV smile or skew. The collection of all IV smiles constitutes the implied volatility surface, i.e., the two-dimensional mapping  $\hat{\sigma} : (K, T) \mapsto \hat{\sigma}(K, T)$ .

Figure 1 portrays the implied volatilities calculated from mid prices of SPX options as of January 23, 2020, across all listed regular expiries and in forward-moneyness  $K/F(0, T)$  space, where  $F(t, T)$  denotes the price specified in a contract at time  $t$  to be paid at time  $T$  for the underlying asset, i.e., the forward price. The IV smiles are clearly violating the Black-Scholes assumption of constant volatility and reflecting the stylized facts of IV [17]. In fact, the implied volatility smiles show large curvature for short expiries that progressively flattens out for longer-dated options. Additionally, the at-the-money-forward (ATMF) term structure of implied volatility is upward sloping.

We follow a parametric approach for the construction of implied volatility surfaces.<sup>1</sup> Thereby, a single non-linear parametric function for the entire surface, or typically for each smile, is defined and fitted to market data [17]. An example of such an approach is the stochastic volatility inspired (SVI) parametrization of [19] based on the large-time asymptotic behavior of the IV smile generated by the Heston model [20]. In our application, we rely on the eSSVI parametrization of total implied variance, proposed in [28]. This approach extends the surface SVI<sup>2</sup>

<sup>1</sup>Note that non- and semi-parametric approaches have also been presented in the literature. An interpolation technique based on convex polynomials that requires the data to be arbitrage-free from the outset is presented in [33]. Natural cubic splines that smooth call prices and do not expect arbitrage-free input data are employed in [16].

<sup>2</sup>SSVI has several attractive features. For example, the term structure of the ATMF implied volatility may be seen as a (vector) parameter of the volatility surface [21]. As such, it does not need to be calibrated and can be observed directly from traded options for a finite set of expiries. Moreover, another desirable property is the existence of tractable no-arbitrage conditions [28].

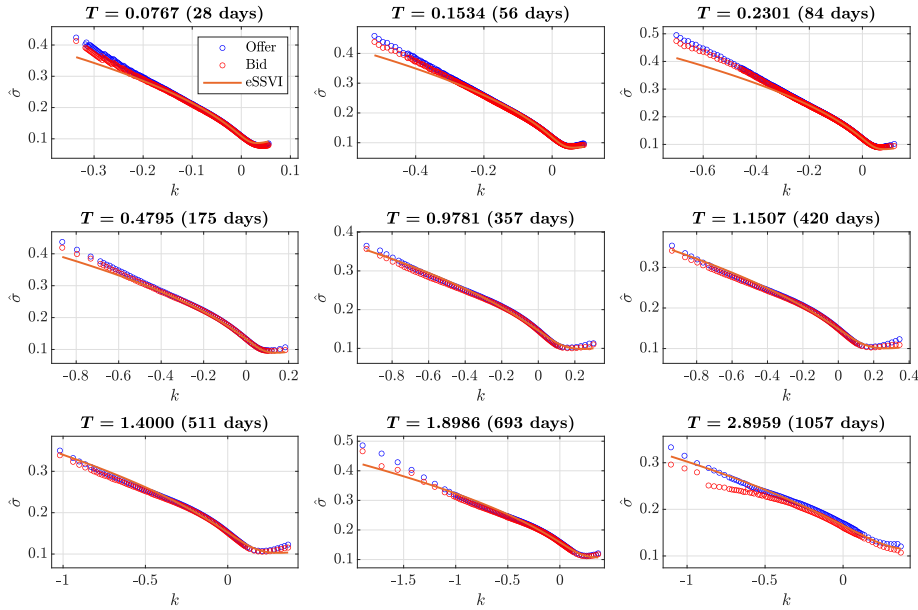


FIGURE 2. eSSVI smiles fit to regular S&P 500 index options as of January 23, 2020, in log-forward-moneyness  $k$  and implied volatility  $\hat{\sigma}$  space. Red and blue circles are bid and offer implied volatilities, respectively, and the orange line presents the eSSVI fit.

(SSVI) model from [21], hence the acronym eSSVI, by making the parameter controlling the rotation of the smile maturity dependent. The formulation of the eSSVI parametrization is provided in Appendix A.3.

Figure 2 depicts the quality of the fit of eSSVI across 9 listed regular SPX expiries as of January 23, 2020. Observe that the fit is generally good, except for the short-term deep out-of-the-money (OTM) put wing.

**3. Local-stochastic volatility.** Local-stochastic volatility was first introduced in [32] with the purpose of creating a model capable of recovering the vanilla smile while maintaining its realistic dynamics to correctly price exotic path-dependent derivatives. The hybrid LSV model aims to combine the advantages of LV and SV models while eliminating their drawbacks [31].

We consider a Heston-like LSV model that is, under the risk-neutral probability measure  $\mathbb{Q}$ , given by the following system of stochastic differential equations (SDEs):

$$dS(t) = (r(t) - q(t))S(t)dt + L(t, S(t))\sqrt{V(t)}S(t)dW^S(t), \quad (1)$$

$$dV(t) = \kappa(\theta - V(t))dt + \eta\sqrt{V(t)}dW^V(t), \quad (2)$$

$$dW^S(t)dW^V(t) = \rho dt, \quad (3)$$

where  $r(t)$  and  $q(t)$  are the deterministic, time-varying, continuously compounded risk-free interest rate and dividend yield inclusive of the borrow rate, respectively,  $\kappa, \theta, \eta, V_0 \in \mathbb{R}_+$  denote the classic Heston parameters [30],  $W^S(t)$  and  $W^V(t)$  are  $\mathbb{Q}$ -Brownian motions,  $\rho \in (-1, 1)$  is the instantaneous correlation between  $W^S(t)$  and  $W^V(t)$ , and  $L(t, S(t))$  is the state-dependent LV correction known as the leverage

function [44]. The parameter  $\kappa$  controls the speed of mean reversion,  $\theta$  is the long-term level of variance, and  $\eta$  is the volatility of variance. The initial level of variance  $V(0) = V_0$  is not observable and thus is treated as a model parameter. The process  $V(t)$  remains positive and can reach 0 only if the so-called Feller condition,  $2\kappa\theta > \eta^2$ , is violated.

Equation (1) implies that the product  $L(t, S(t))\sqrt{V(t)}$  gives the overall instantaneous volatility in the model [6]. The stochastic process  $V(t)$  in Eq. (2) is responsible for matching the dynamics of the implied volatility smile, whereas the deterministic component  $L(t, S(t))$  is introduced to recover the market implied volatility surface [32].

In the local volatility model, the SDE governing the risk-neutral diffusive evolution of the current price of the underlying asset  $S(t)$  is given by

$$dS(t) = (r(t) - q(t))S(t)dt + \sigma_{LV}(t, S(t))S(t)dW^S(t), \quad (4)$$

where  $\sigma_{LV}(t, S)$  is the state-dependent diffusion coefficient known as the local volatility function. The expression relating the function  $\sigma_{LV}(t, S)$  to European option prices and their strike and maturity derivatives is given by [15] and [13]. Assume that European call prices  $C(K, T) = e^{-\int_0^T r(u)du} \mathbb{E}^\mathbb{Q}[(S(T) - K)^+]$  are known for a continuum of maturities  $T$  and strikes  $K$ . Then, by the so-called Dupire's formula, the local volatility function is given by

$$\sigma_{LV}^2(t, S) = 2 \frac{\frac{\partial C}{\partial T} + (r(T) - q(T))K \frac{\partial C}{\partial K} + q(T)C}{K^2 \frac{\partial^2 C}{\partial K^2}} \Big|_{T=t, K=S}. \quad (5)$$

The proof of Eq. (5) is outlined, e.g., in [13] and [19]. From a given spectrum of European option prices, with any strike  $K \geq 0$  and expiry  $T \geq 0$ , one can employ the right-hand side of Eq. (5) to compute the unique local volatility surface that recovers the market prices of European options.

The LSV model should mimic the LV model so that the two processes have identical one-dimensional marginal distributions and the prices of European options match for all strikes  $K$  and expiries  $T$  [37]. Using the Gyöngy's theorem on mimicking processes, see [25] and Appendix A.1, we can match the diffusion terms of Eqs. (1) and (4) by

$$\sigma_{LV}(t, S) = \sqrt{\mathbb{E}^\mathbb{Q}[L(t, S(t))^2 V(t) | S(t) = S]}.$$

Rearranging the above equation, and because  $L(t, S)$  is a deterministic function of  $t$  and  $S$ , we can obtain the expression for the leverage function:

$$L(t, S) = \frac{\sigma_{LV}(t, S)}{\sqrt{\mathbb{E}^\mathbb{Q}[V(t) | S(t) = S]}} = \sigma_{LV}(t, S) \sqrt{\frac{\int_{\mathbb{R}_+} p(t, S, V) dV}{\int_{\mathbb{R}_+} V p(t, S, V) dV}}, \quad (6)$$

where  $p(t, S, V)$  denotes the transition probability density function of the LSV model [43]. Because the joint distribution of  $S(t)$  and  $V(t)$  is unknown, a closed-form representation of Eq. (6) for the Heston LSV model is not available [45]. The calibration procedure of  $L(t, S)$  is presented in Appendix A.3. Note that Eq. (6) can

intuitively be seen as a ratio between local volatility and the conditional expectation of stochastic volatility.<sup>3</sup>

By construction, the prices of European options under the LSV model always match the prices under the pure LV model. Therefore, even if the pure SV model fails to recover the market data, the LV correction compensates for this. Given this feature, we are allowed to study the sensitivity of any complex derivatives price with respect to the SV model parameters such as the volatility of variance  $\eta$  or the spot-variance correlation  $\rho$ , while preserving an exact fit to the IVS.

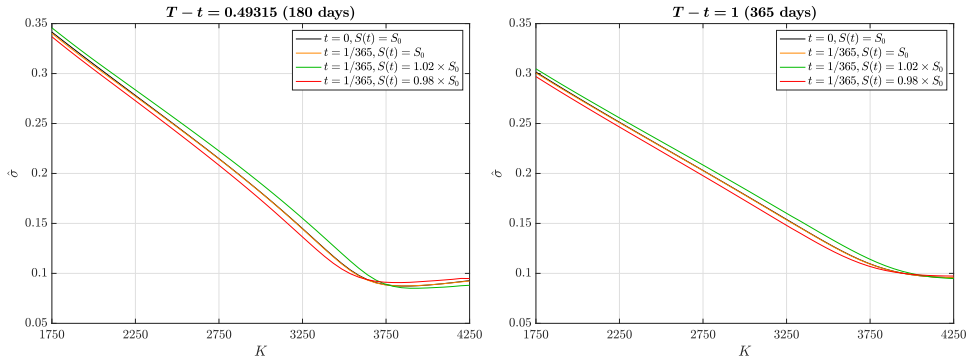


FIGURE 3.  $T - t = 180$  and  $365$  days IV smile dynamics in the Heston LSV model calibrated to SPX options as of January 23, 2020. In black the current IV smile. In orange, green, and red the forward IV smiles resulting from different levels at time  $t = 1/365$ .

Figure 3 shows that the Heston LSV model captures the correct dynamics of the IV smile and the typical market behavior, i.e., the fact that the skew moves in the same direction as the underlying level. In fact, in contrast to what we observed for the LV model, the IV smile shifts to the right for an increase in the index level and vice versa for a decrease [26].

Figure 4 allows us to observe that the forward-starting IV smiles generated by the Heston LSV model are approximately time-homogeneous. Indeed, with increasing  $T_1$ , the skew is persisted; the forward IV smile is consistent with today's IV smile. This represents a great advantage of the LSV model in comparison to the commonly-employed LV model [38].

The limitation of the LSV model is the non-trivial and computationally demanding calibration of the leverage function. Moreover, since the diffusion term in Eq. (1) does not only depend on the current value of  $S(t)$  but also on its probability distribution, the SDE is non-linear and [24] argue that the existence of an LSV model for a given market IVS is not guaranteed, despite the opposite being a widespread belief in the quantitative finance community.

Yet, the Heston LSV model represents a suitable model for pricing the vol-of-vol and the forward-smile risk. Autocallable structured notes are sensitive to these risks due to their high path- and model-dependency. In the following section, the focus

<sup>3</sup>The model specifications directly imply two limiting cases. When  $L(t, S) = 1$ , for all  $S$  and  $t$ , the LSV model collapses to a pure SV model. Similarly, when  $\eta = 0$ , the process  $V(t)$  becomes deterministic, we have  $L(t, S) = \sigma_{LV}(t, S)/\sqrt{V(t)}$  and hence the LSV model boils down to a pure LV model [32].

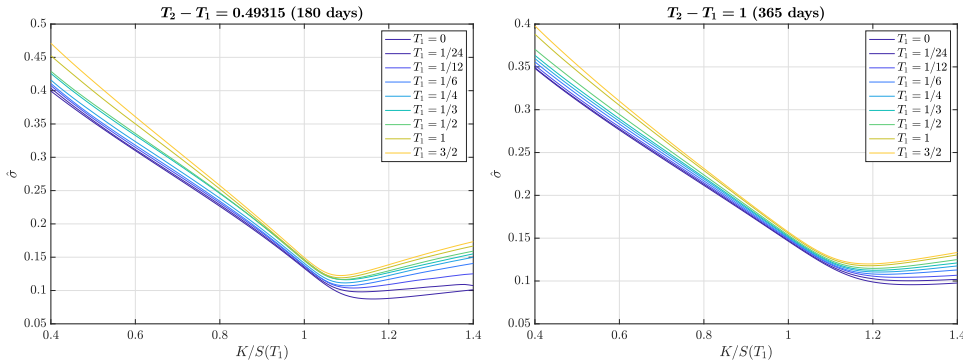


FIGURE 4. 180 and 365 days spot- and forward-starting implied volatility smiles generated by the Heston local-stochastic volatility model calibrated to SPX options as of January 23, 2020.  $T_1$  denotes the forward start date and  $T_2 - T_1$  the residual maturity.

is set on the comparison of the prices of such derivatives under the LV model and the Heston-like LSV model.

**4. Autocallables pricing.** This section investigates the popular class of structured notes (SNs), known as autocallable barrier reverse convertibles (ABRCs). In particular, we compare the pricing of such exotic derivatives in the LV versus the Heston LSV model. SNs are generally issued at 100% of their face value, where a margin is included in the issue price. In this paper, we focus on the theoretical values and thus exclude trading spreads, barrier shifts, and sales margins. Moreover, payoffs are discounted with risk-free rates, thus ignoring issuers' credit risk.

**4.1. Payoff definition and risks.** The structure of an ABRC can assume different features and be defined with several distinct characteristics. The typical BRC can be decomposed into a zero-coupon bond (ZCB), a short D&I put option, and a stream of coupons. The latter can be: i) contingent on the underlying asset prices observed at specific intermediate dates, i.e., be subject to down-and-out (D&O) barriers and thus be decomposed into a strip of digital call options, or ii) guaranteed. Autocall denotes the enhancement with an early termination feature in the form of Bermudan U&O barriers, which, if hit, lead to the immediate repayment of the face value of the SN in addition to a coupon payment. We consider the features presented in Table 1.

Consider the set of observation dates  $\mathcal{T} = \{T_1, \dots, T_N\}$ , where  $T_1 = T^O$  and  $T_{i+1} - T_i = T^O$ , for  $i = 1, \dots, N - 1$ . Define  $i^* := \inf\{i = 1, \dots, N - 1 | S(T_i) \geq S(0)H_i^{AC}\} \wedge N$ , and  $L := \min_{T \in [0, T_N]} \{S(T)\}$  or  $L := S(T_N)$  if the knock-in barrier  $H$  is observed continuously or only at the final valuation date  $T_N$ , respectively.

The final payoff of the ABRC for one unit of notional at time  $T_{i^*}$ , which is either the early redemption date or the final valuation date, is given by

$$h(T_{i^*}) = 1 + \begin{cases} \mathbb{1}_{\{S(T_N) \geq S(0)H_N^{AC}\}} Y_N^{AC} - \mathbb{1}_{\{L \leq S(0)H\}} \frac{1}{K} \left(K - \frac{S(T_N)}{S(0)}\right)^+, & T_{i^*} = T_N \\ Y_{i^*}^{AC}, & T_{i^*} < T_N \end{cases}.$$

The final payoff consists of the face value of the ZCB, the autocall coupon (if any), and, in case  $T_{i^*} = T_N$  (i.e., no early redemption occurs), the payout of the short

Feature	Notation	Description
Expiry tenor	$T^E$	Tenor corresponding to the final valuation date of the SN expressed in months, e.g., 12 months.
Observation tenor	$T^O$	Tenor corresponding to the length of the observation periods expressed in months, i.e., the time intervals between the dates at which the coupon barrier and autocall barrier are observed, e.g., 3 months.
Strike	$K$	Strike of the short put option expressed in % of the current spot $S(0)$ , e.g., 90%. The gearing of the put option is given by $1/K$ .
Knock-in barrier	$H$	D&I barrier level expressed in % of $S(0)$ , e.g., 80%. If hit, it knocks-in the short put option. It can be observed only at the final valuation date (European) or continuously (American).
Coupon	$Y$	Coupon level paid at the end of each observation period if the coupon barrier is not hit, e.g., 3% per annum (p.a.).
Coupon barrier	$\mathbf{H}^Y$	D&O barrier levels expressed in % of $S(0)$ , e.g., 80%. If hit, they invalidate or delay the coupon payment. They can be constant or variable and are observed at the end of each observation period.
Autocall coupon	$\mathbf{Y}^{AC}$	Coupon levels paid upon early redemption expressed in percentage of the notional, e.g., 3%. They can be constant or “snowballing”.
Autocall barrier	$\mathbf{H}^{AC}$	U&O barrier levels expressed in % of $S(0)$ , e.g., 100%. If hit, they trigger the early redemption of the SN. They can be constant or “step-down” and are observed at the end of each period (Bermudan).

TABLE 1. Description of the main features determining the ABRC.  $T^E, T^O, K, H$ , and  $Y$  are scalars.  $\mathbf{H}^Y, \mathbf{Y}^{AC}$ , and  $\mathbf{H}^{AC}$  are  $N \times 1$  vectors, where  $N = T^E/T^O$  is the number of observation dates.

D&I put option. Additionally, at the  $i$ -th observation date  $T_i$ , for  $i = 1, \dots, i^*$ , the holder of the ABRC receives the following coupon amount:

$$M(i)\mathbb{1}_{\{S(T_i) > S(0)H_i^Y\}}Y,$$

where, if the coupon barrier has the so-called “memory” feature, we have  $M(1) = 1$  and  $M(j) = j - \sup\{i = 1, \dots, j-1 | S(T_i) > S(0)H_i^Y\} \vee 0$  for  $j > 1$ . Therefore,  $M(i) - 1$  corresponds to the number of foregoing missed coupon payments at time  $T_i$ . If the coupon barrier has no memory, we have  $M(j) = 1$  for all  $j \geq 1$ .

Thus, the fair value of the ABRC at time  $t = 0$ , denoted by  $U(0)$ , is given by the risk-neutral expectation of the discounted future coupon payments and the final payoff:

$$U(0) = \mathbb{E}^{\mathbb{Q}} \left[ e^{-\int_0^{T_{i^*}} r(u)du} h(T_{i^*}) + \sum_{i=1}^{i^*} e^{-\int_0^{T_i} r(u)du} M(i)\mathbb{1}_{\{S(T_i) > S(0)H_i^Y\}}Y \right]. \quad (7)$$

Notice that  $U$  is path-dependent and  $T_{i^*}$  is a stopping time. Moreover, the BRC is a special case of ABRC with  $\mathbf{H}^{AC} = \infty$  and hence  $T_{i^*} = T_N$ .

Consider the following ABRC on SPX priced as of January 23, 2020, and denominated in USD as our benchmark example:  $T^E = 12$ ,  $T^O = 3$ ,  $K = 1.00$ ,  $H = 0.80$  and European,  $Y = 7.19\%$  p.a. as it leads to  $U^{LV}(0) = 1$ ,  $\mathbf{H}^Y = \mathbf{0}$  and thus the coupon is guaranteed,  $\mathbf{Y}^{AC} = \mathbf{0}$ ,  $\mathbf{H}^{AC} = \mathbf{1}$ , and  $N = 4$ .

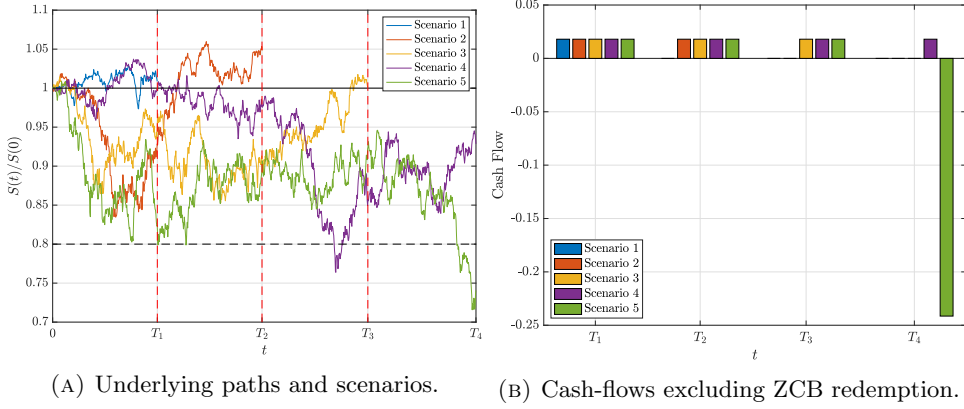


FIGURE 5. Different ABRC payoff scenarios for  $T^E = 12$ ,  $T^O = 3$ ,  $K = 1.00$ ,  $H = 0.80$  European,  $Y = 7.19\%$  p.a.,  $\mathbf{H}^Y = \mathbf{0}$ ,  $\mathbf{Y}^{AC} = \mathbf{0}$  and  $\mathbf{H}^{AC} = \mathbf{1}$ .

Figure 5 illustrates the scenarios for different paths of the underlying level. In Scenario 1, the underlying level at the observation date  $T_1$  is above the autocall barrier, i.e.,  $S(T_1) \geq H_1^{AC}S(0)$ . Therefore, the note is early redeemed at time  $T_1$  with 100% payoff and a coupon payment of  $\frac{1}{4} \times 7.19\%$  of the notional amount. Scenarios 2 and 3 are similar to the latter, however, the autocall barrier is breached at times  $T_2$  and  $T_3$ , respectively. This implies that two and three coupon payments amounting each to  $\frac{1}{4} \times 7.19\%$  are received by the note holder at times  $T_1, T_2$  and  $T_1, T_2, T_3$ , respectively. In Scenarios 4 and 5,  $S(T_i) < H_i^{AC}S(0)$ , for  $i = 1, 2, 3$ , and thus the note holder receives all the coupon payments at times  $T_1, T_2, T_3$ , and  $T_4$ . In Scenario 4,  $S(T_4) > HS(0)$ , hence the note holder receives 100% of the face value. Whereas in Scenario 5,  $S(T_4) \leq HS(0)$  and the note holder participates 1:1 to the negative performance of the underlying incurring a loss.

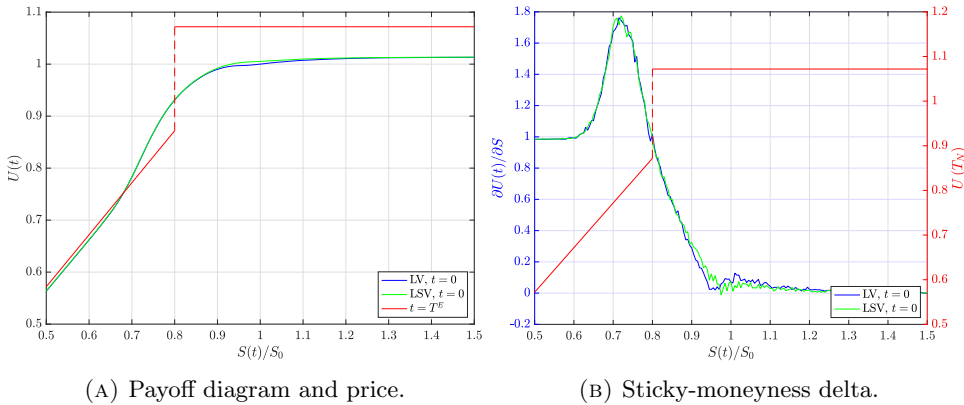


FIGURE 6. Payoff diagram, price, and sticky-moneyness delta at the inception of the benchmark ABRC for different  $S$  at  $t = 0$ .

Figure 6a exhibits the LV and Heston LSV price of the ABRC for different levels of  $S$  at time  $t = 0$ . Due to the short D&I put option, the holder is short volatility

and skew at the inception of the trade. Indeed, higher volatility and skew increase the probability of reaching the barrier  $H$  and the option to end ITM [8]. The exposure to the forward is long, which means that the holder is long the underlying asset level and short dividends, see Fig. 6b. In fact, a higher forward implies a lower probability of reaching the barrier  $H$  and the option to end ITM at expiry. Figure 6b also shows that the gamma  $\frac{\partial^2 U}{\partial S^2}$  exposure is not single-signed. Remember that the issuer of the note takes the opposite risks on its books.

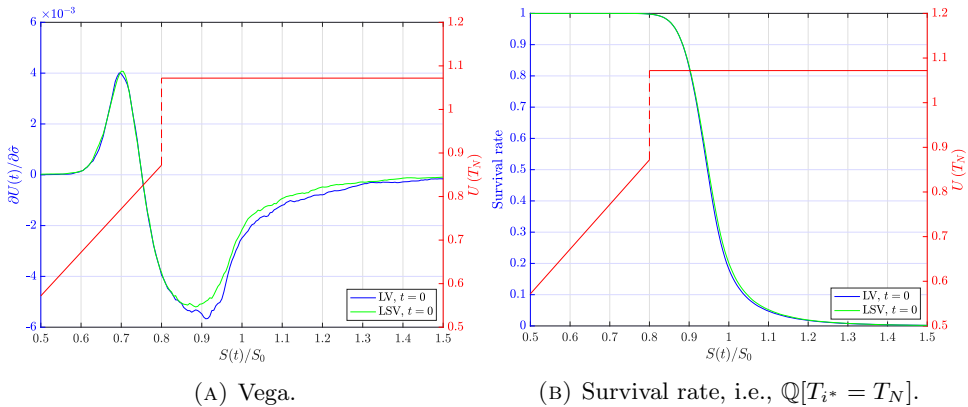


FIGURE 7. Vega computed with a parallel shift of the IVS, and survival rate of the benchmark ABRC for different  $S$  at  $t = 0$ .

Autocallables are known to have a strong model-dependency due to the cancellable feature implied by the Bermudan U&O barriers. Consequently, static replication is not possible, and dynamic re-hedging with vanilla options is required as the underlying level moves [42].

As shown in Fig. 7, the paths of the underlying level relative to the barrier levels are driving the vega dynamics of autocallables. In fact, as the underlying level falls, vega decreases initially and then increases to turn positive below the D&I barrier, see Fig. 7a. On the other hand, as the underlying level rises, vega tends towards zero because the early redemption of the note becomes more likely. Figure 7b suggest that the volatility exposure is also highly dynamic in the tenor dimension. This generates significant vega re-hedging costs for the issuers. As a matter of fact, a pricing model capable of capturing a realistic spot-volatility covariance, which is a known deficiency of the LV model, is essential [42].

We observe in Fig. 6a that the price of the ABRC obtained using the Heston LSV model is strictly higher than the LV price, whereby the difference attains a maximum at around 97.50% of the current spot. In the subsequent sections, we analyze this closely.

Our price estimates are obtained by evaluating the expectation in Eq. (7) with QMC methods, whereby Sobol sequences of low-discrepancy quasi-random numbers are used. To ensure the comparability of the QMC estimates of the derivatives prices between the two models, we employ the same quasi-random sequences, an equidistant time-grid with  $m = 1000$  transition steps, and  $n = 2^{15}$  paths as inputs for the simulations. For additional information see Appendices A.2 and A.3. For variance reduction of the simulation estimates, we use the method of antithetic

variates across the two models. The discussion of these methods goes beyond the scope of this paper and is left to the interested reader, for example, see [22].

**4.2. Structure sensitivity.** Here, we investigate which features from Table 1 lead to price differences between the LV and Heston LSV models and thus we determine which elements possess the highest model-dependency and exposure to the vol-of-vol and the forward-smile risk. The assumed benchmark structure is that of Section 4.1, with extended  $T^E$ . The coupon level  $Y$  is computed for each  $T^E$  such that  $U^{LV}(0) = 1$ , leading to the results displayed in Table 2.

$T^E$	3	6	9	12	15	18	21	24	30	36	42
$Y$	3.99%	5.94%	6.85%	7.19%	7.18%	7.21%	7.12%	7.01%	6.80%	6.55%	6.31%
$T^E$	48	54	60	66	72	78	84	90	96	108	120
$Y$	6.08%	5.86%	5.73%	5.55%	5.40%	5.26%	5.13%	5.01%	4.87%	4.68%	4.53%

TABLE 2.  $Y$  for different  $T^E$  computed as of January 23, 2020.

For the base payoff, the valuation difference, which we define as  $\Delta^{LSV} := U^{LSV}(0) - U^{LV}(0)$ , is driven uniquely by the autocall feature. In fact, leaving this aside, the payoff uniquely depends on the marginal distribution of  $S(T_E)$ , which is by construction the same under the two models.

Because of the path-dependent nature of ABRCs, we expect to find  $\Delta^{LSV} > 0$ . We proceed below with testing our claim by changing or adding some features while keeping the rest of the benchmark structure unchanged.

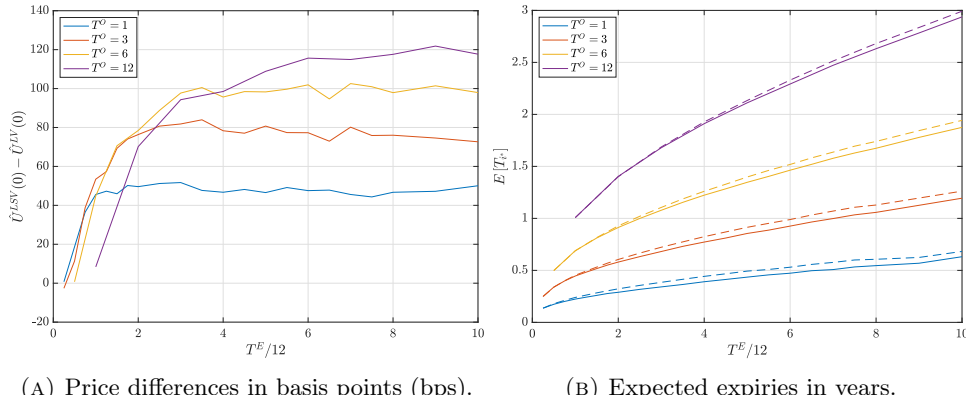


FIGURE 8.  $\hat{U}^{LSV}(0) - \hat{U}^{LV}(0)$  and  $E^Q[T_{i^*}]$  for different observation tenors  $T^O$  and across different expiry tenors  $T^E$ . In the right panel, the solid line is for LV and the dashed line for Heston LSV.

Figure 8a confirms our expectations as we observe  $\hat{U}^{LSV}(0) > \hat{U}^{LV}(0)$  for all  $T^E$  and  $T^O$ . For the base case  $T^O = 3$ , the price difference is around 10 bps at  $T^E = 6$  and increases rapidly to reach a constant level of approximately 80 bps at the 3 years expiry tenor. The same is for  $T^O = 1, 6$ , and 12, whereby the price differences settle around 50, 100, and 120 bps, respectively. In fact, the price differences demonstrate to be larger for longer  $T^O$  and tend to be positively related

to the expected expiry  $\mathbb{E}^{\mathbb{Q}}[T_{i^*}]$ . This makes intuitive sense since the shorter the expected expiry is, the smaller the impact of the decaying future ATMF skews in the LV model on the dynamical properties of  $S(t)$  is.

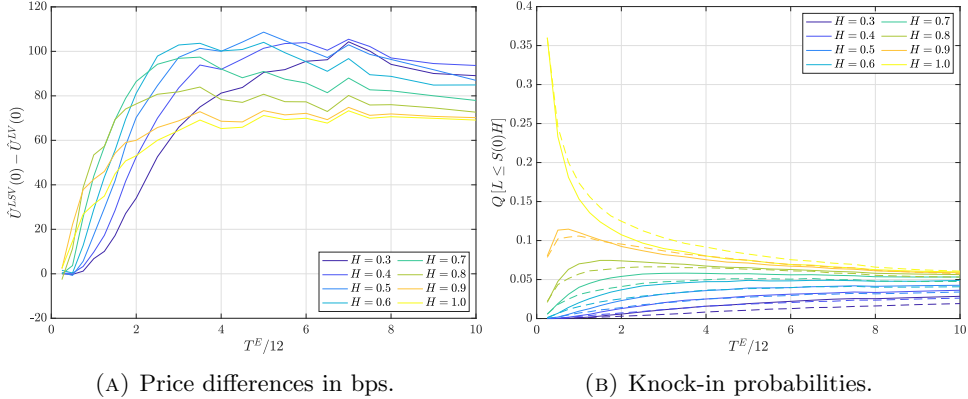


FIGURE 9.  $\hat{U}^{LSV}(0) - \hat{U}^{LV}(0)$  and  $\mathbb{Q}[L \leq S(0)H]$  for different barriers  $H$  and across different expiry tenors  $T^E$ . In the right panel, the solid line is for LV and the dashed line for Heston LSV.

Figure 9a shows that  $\Delta^{LSV} > 0$ , for all  $T^E$  and  $H$ . Moreover, for short tenors,  $\Delta^{LSV}$  decreases with decreasing  $H$ . This trend then progressively reverses for longer  $T^E$  such that  $\Delta^{LSV}$  decreases with higher  $H$ . The knock-in probabilities are, except for  $H = 0.9, 1$ , marginally higher under the LV model, see Fig. 9b.

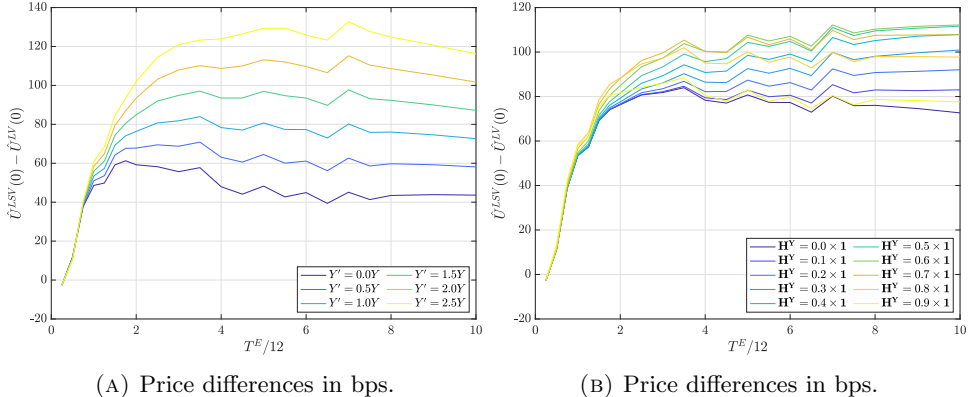


FIGURE 10.  $\hat{U}^{LSV}(0) - \hat{U}^{LV}(0)$  in bps for different coupon levels  $Y'$ , left panel, and coupon barrier levels  $\mathbf{H}^Y$  without memory, right panel, across various expiry tenors  $T^E$ .

Figure 10a exhibits that  $\Delta^{LSV}$  scales linearly with the coupon level. From Fig. 10b, we observe that for a fixed  $T^E$ ,  $\Delta^{LSV}$  is a concave function of  $\mathbf{H}^Y$ . Indeed, a maximum is attained at  $\mathbf{H}^Y = 0.6 \times \mathbf{1}$ , while, for  $\mathbf{H}^Y < 0.6 \times \mathbf{1}$  and  $\mathbf{H}^Y > 0.6 \times \mathbf{1}$ ,  $\Delta^{LSV}$  decreases. The guaranteed coupon case, i.e.,  $\mathbf{H}^Y = \mathbf{0}$ , defines the lower boundary for  $\Delta^{LSV}$ . As a result, the coupon barrier generally increases  $\Delta^{LSV}$  and hence the structure's model-dependency.

The impacts of the autocall coupon and the autocall barrier level are analyzed in Appendix B.1. All in all, the results presented in this section suggest that the features of the structure and their effect on the model-dependency and exposure to the vol-of-vol as well as the forward-smile risk should be taken into consideration when pricing and risk-managing ABRCs.

**4.3. Parameter sensitivity.** Here, we assess the sensitivity of the ABRC's LSV valuation with respect to the Heston parameters.<sup>4</sup> We consider the same benchmark structure on SPX as defined in Section 4.1.

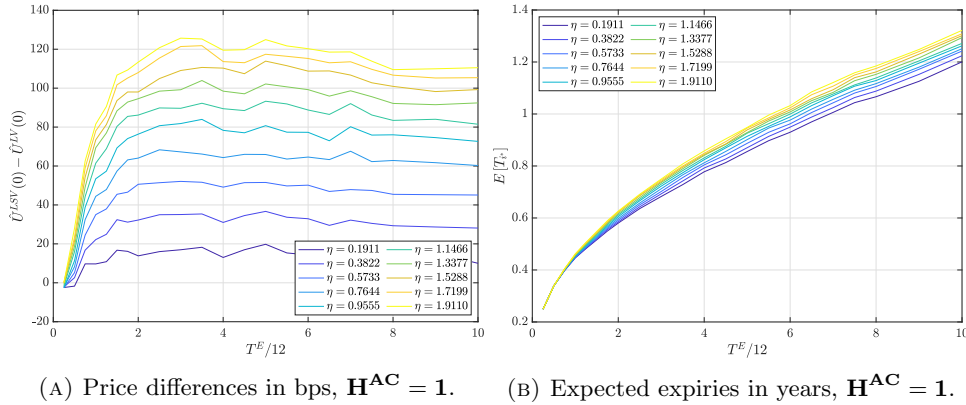


FIGURE 11.  $\hat{U}^{\text{LSV}}(0) - \hat{U}^{\text{LV}}(0)$  for different volatility of variance levels  $\eta$  across various expiry tenors  $T^E$ . In the right panel, the corresponding Heston LSV expected expiries  $\mathbb{E}^{\mathbb{Q}}[T_{i^*}]$ .

Figure 11 portrays  $\Delta^{\text{LSV}}$  for different levels of  $\eta$ , i.e., the volatility of variance parameter. As expected, larger values of  $\eta$  lead to higher price differences between the Heston LSV and LV models, in addition to longer  $\mathbb{E}^{\mathbb{Q}}[T_{i^*}]$ . This confirms the sensitivity of autocallable derivatives to the vol-of-vol and forward-smile risk, see also Fig. 12a. As  $\eta \rightarrow 0$ , we see that  $\Delta^{\text{LSV}} \rightarrow 0$  since, by construction, the LSV model converges to the LV model. Moreover, we observe that the impact of higher  $\eta$  on  $\Delta^{\text{LSV}}$  becomes progressively smaller.

Next, we study the influence of  $\eta$  on the forward IV smiles. Figure 12a shows that the forward ATM skew steepens with increasing  $\eta$ . Therefore, the future volatility of implied volatilities rises with  $\eta$ . On the other hand, the forward ATM implied volatility levels decrease with higher  $\eta$ , thus implying higher prices in accordance with the ABRC's short volatility exposure for the note holder.

Figure 13 suggests that  $\Delta^{\text{LSV}}$  decreases with higher spot-variance correlation levels, whereas the expected time to expiry lengthens. The price differences are nearly linear in  $\rho$  and constant across  $T^E$ . The influence of increasing  $\rho$  can be explained by a flatter forward ATM IV skew and the lower close to ATM forward IVs, see Fig. 12b. Intuitively, as the underlying level moves higher, the volatility decreases by a larger extent for lower correlations. This phenomenon is reflected by the lower forward-starting IVs in the call wing. Hence, with lower volatility,

<sup>4</sup>In principle, we could also alter the eSSVI surface parameters and explore the results. However, the fit to European call and put option market prices would be compromised.

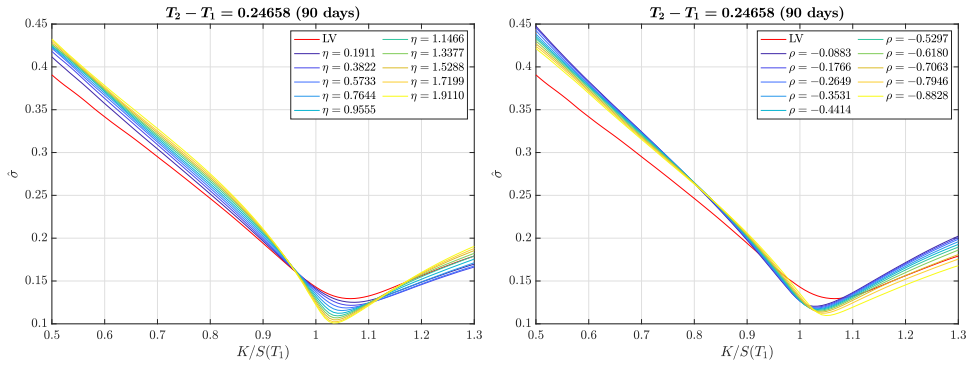


FIGURE 12.  $T_1 = 3$  months forward-starting IV smiles generated by the Heston-like LSV model calibrated to SPX option as of January 23, 2020, for different levels of Heston parameters  $\eta$  and  $\rho$ .

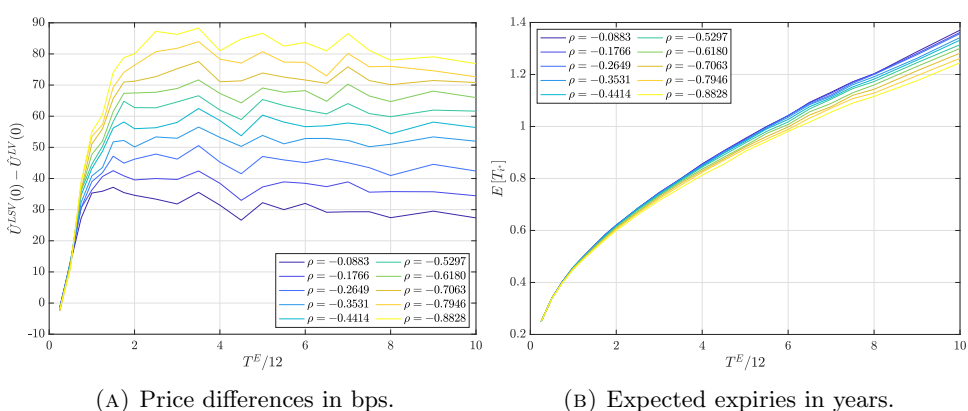


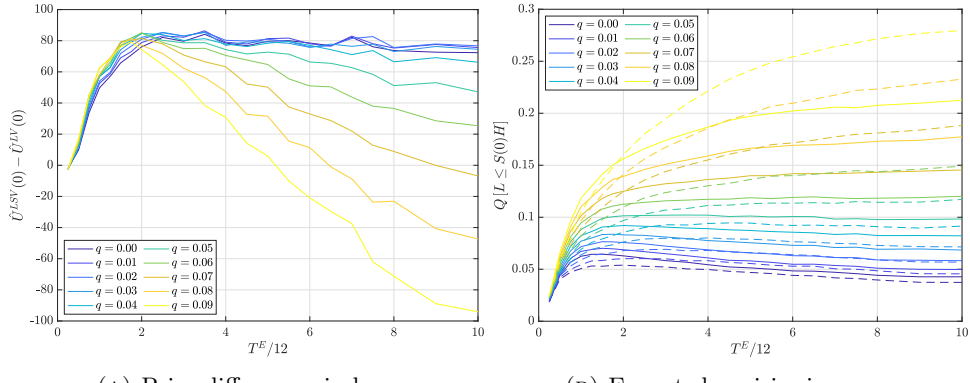
FIGURE 13.  $\hat{U}^{LSV}(0) - \hat{U}^{LV}(0)$  for different correlation levels  $\rho$  across various expiry tenors  $T^E$ . In the right panel, the corresponding Heston LSV expected expiries  $\mathbb{E}^{\mathbb{Q}}[T_{i^*}]$ .

the early redemption and knock-in probabilities increase and decrease, respectively, while pushing the ABRC valuations higher.

The sensitivity of the ABRC's price with respect to the speed of mean reversion  $\kappa$ , the long-term variance level  $\theta$ , and the initial level of variance  $V_0$  are analyzed in Appendix B.2. The main takeaway of this section is that the Heston LSV model allows us to control for the spot-implied volatility dynamics through the SV parameters whilst recovering European call and put option prices and effectively impacting the prices of exotic derivatives.

**4.4. Underlying sensitivity.** Here, we assess underlying specific sensitivities of the valuation differences of ABRCs between the Heston LSV and the LV models. First, we test the impact of different forward levels on the benchmark structure referencing SPX. Second, we study the degree of model dependence across different underlyings. We consider the following indices: SPX, NDX, DAX, and RUT. These

indices represent popular choices for investors seeking exposure to the US market via ABRCs. The studied benchmark structure remains that of Section 4.1.



(A) Price differences in bps. (B) Expected expiries in years.

FIGURE 14.  $\hat{U}^{LSV}(0) - \hat{U}^{LV}(0)$  and  $Q[L \leq S(0)H]$  for different dividend yields  $q$  and across different  $T^E$ . In the right panel, the solid line is for LV and the dashed line for Heston LSV.

We compute the SPX ABRC prices assuming different constant and continuously compounded dividend yields  $q \in \{0.00, 0.01, \dots, 0.09\}$ . The results are displayed in Fig. 14a and suggest that, for short expiry tenors  $T^E < 24$ ,  $\Delta^{LSV}$  is positive and slightly increasing with  $q$ . Beyond  $T^E \approx 24$ , however,  $\Delta^{LSV}$  decreases with lower forward prices. Moreover, for  $q \geq 0.07$ ,  $\Delta^{LSV}$  even becomes negative for sufficiently large  $T^E$ , indicating that Heston LSV prices fall below LV prices. Figure 14b exhibits the knock-in probabilities, namely  $Q[L \leq S(0)H]$ . As the observation suggests and as discussed in Section 4.1, the probability of breaching the D&I barrier decreases with the forward level. Interestingly, the LV model generally implies higher knock-in probabilities than the Heston LSV model for  $T^E < 24$ , whereas the opposite holds true for  $T^E \geq 24$ . This explains the evolution of  $\Delta^{LSV}$  along  $T^E$ .

$T^E$	3	6	9	12	15	18	21	24	30	36	42	
NDX	Y	5.15%	7.25%	8.02%	8.31%	8.27%	8.13%	7.93%	7.78%	7.39%	7.06%	6.81%
DJX	Y	3.56%	5.61%	6.70%	7.18%	7.32%	7.29%	7.20%	7.08%	6.85%	6.55%	6.31%
RUT	Y	4.65%	6.70%	7.56%	7.84%	7.83%	7.71%	7.55%	7.45%	7.15%	6.84%	6.55%
$T^E$	48	54	60	66	72	78	84	90	96	108	120	
NDX	Y	6.48%	6.27%	6.05%	5.82%	5.66%	5.50%	5.34%	5.23%	5.09%	4.86%	4.68%
DJX	Y	6.09%	5.92%	5.71%	5.56%	5.43%	5.28%	5.14%	5.03%	4.92%	4.71%	4.54%
RUT	Y	6.27%	6.07%	5.87%	5.69%	5.53%	5.36%	5.23%	5.10%	4.98%	4.77%	4.57%

TABLE 3.  $Y$  for different underlyings and  $T^E$  computed as of January 23, 2020, for the benchmark ABRC.

Next, we study the sensitivity of ABRC valuation given different underlying indices. Appendix B.3 presents the eSSVI and Heston parameters calibrated to SPX, NDX, DJX, and RUT options as of January 23, 2020.

The pricing of the base structure with the same coupon across all indices would lead to biased and uninterpretable results. Therefore, before computing  $\Delta^{LSV}$ , we

calculate the value of the coupon  $Y$  for each underlying such that  $U^{LV}(0) = 1$ , see Tables 2 and 3. Note that, for a fixed tenor  $T^E$ , the coupon is greater for underlyings exhibiting higher IVs, see Appendix B.3. Moreover, to isolate the effect of higher coupons, we also run the calculations for  $Y = 0$ .

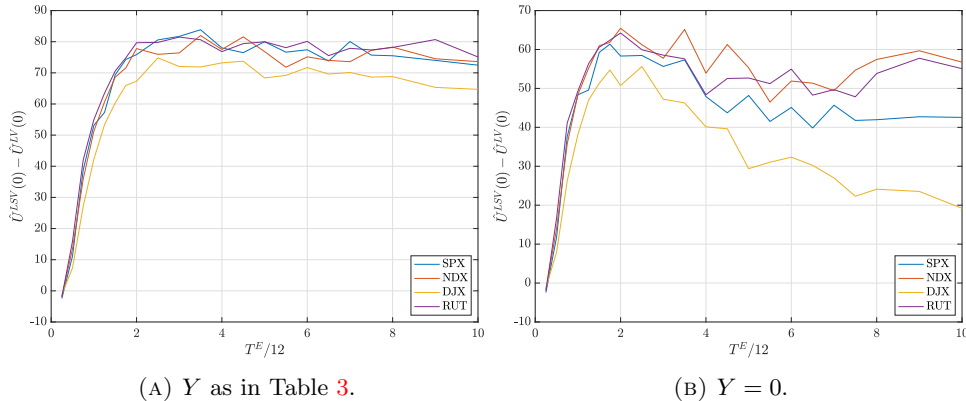


FIGURE 15.  $\hat{U}^{LSV}(0) - \hat{U}^{LV}(0)$  for the indices SPX, NDX, DJX, and RUT across expiry tenors  $T^E$ .

Figure 15 shows  $\Delta^{LSV}$  for the four indices and across different expiry tenors  $T^E$ . In the left panel, the coupon is set according to Table 3, whereas in the right panel it is fixed to  $Y = 0$ . Despite the differences in the Heston parameters, the eSSVI surface, and the coupon amounts, the values of  $\Delta^{LSV}$  are relatively close to each other for SPX, NDX, and RUT, see Fig. 15a. Due to the lower forward,  $\Delta^{LSV}$  is around 10 bps lower for DJX. However, Fig. 15b suggests that, with  $Y = 0$ , an underlying specific pattern arises such that the indices with a higher forward and higher implied volatilities tend to exhibit higher  $\Delta^{LSV}$  and vice versa.

This analysis shows us that underlying-implicit characteristics such as forwards and IV levels do influence the additional cost of ABRCs implied by enhancing LV with an SV component. For instance, lower forward levels increase knock-in probabilities.

**4.5. Market sensitivity.** Finally, we assess how the market environment affects  $\Delta^{LSV}$  by repeating the above analysis on the previously studied benchmark structure. We define four volatility regimes proxied by the VIX level: i) 9.14, i.e., low as of November 3, 2017, ii) 31.37, i.e., medium-low as of June 23, 2020, iii) 53.54, i.e., medium-high as of March 31, 2020, and iv) 75.91, i.e., high as of March 17, 2020.

Observe the significant impact of the market volatility regime on  $\Delta^{LSV}$  in Fig. 16. The low-volatility regime is presented in Figs. 16a and 16b and the high regime in Figs. 16c and 16d. Moreover, Figs. 16a and 16c depict  $\Delta^{LSV}$  for the benchmark structure with the coupon  $Y$  defined such that  $U^{LV}(0) = 1$ , whereas Figs. 16b and 16d show the results for  $Y = 0$ , hence isolating the impact of  $Y$  on  $\Delta^{LSV}$ . Note that the medium-low and medium-high regimes, together with additional results, are presented in Appendix B.4.

For SPX,  $Y = 0$ , and  $T^E = 48$ , we obtain  $\Delta^{LSV} \approx 50, 80, 120$ , and 140 bps in low, medium-low, medium-high, and high volatility markets, respectively. Accounting for the higher coupon levels, the price differences become even more

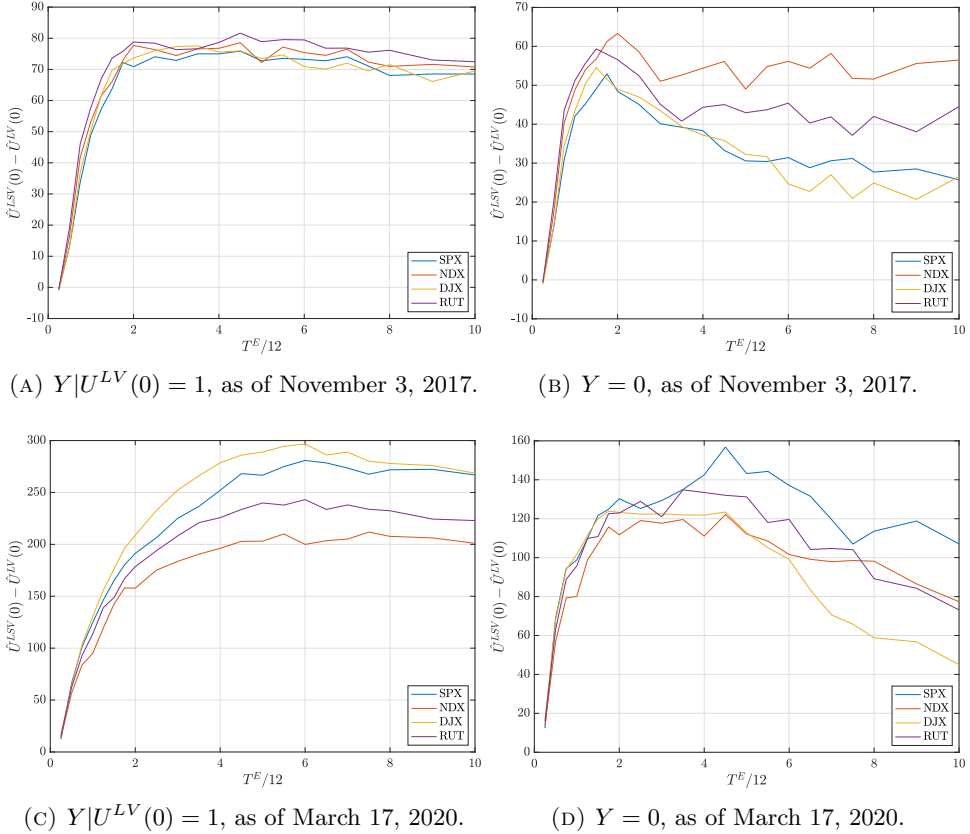


FIGURE 16.  $\hat{U}^{LSV}(0) - \hat{U}^{LV}(0)$  for SPX, NDX, DJX, and RUT across expiry tenors  $T^E$ , in low (subplots a and b) and high (subplots c and d) volatility regimes and for different  $Y$ .

important:  $\Delta^{LSV} \approx 70, 145, 190$ , and  $250$  bps, respectively. This applies directly to the other indices as well. Notice also that  $\Delta^{LSV}$  tends to be more spread out across the indices in highly volatile markets. This indicates that underlying specific characteristics assume more weight. Furthermore, high implied volatility and high forward imply larger model valuation differences, in line with Section 4.4.

Figure 17 depicts the evolution of  $\Delta^{LSV}$  for the  $T^E = 12$  benchmark structure on SPX over the period spanning from January 3, 2017, to December 31, 2020. Observe a significant positive relationship between the VIX level, the coupon  $Y$ , and the model valuation differences  $\Delta^{LSV}$ . The price differences amount on average to 60 bps for the ABRC under consideration. The minimum and maximum  $\Delta^{LSV}$  are 37 and 130 bps, respectively, and the standard deviation is 14 bps.

This observation is only partially explained by higher coupons that can be obtained by selling a more expensive put option in periods of high implied volatilities, compare the black and the blue line in Fig. 17. Indeed, the main drivers are the higher volatility-of-variance and lower spot-variance correlation (see Section 4.3.) resulting from the calibration of the Heston model in stressed markets.

The results show that the model-dependency implicit in autocallable derivatives and reflected in the valuation differences is tied to market's implied volatility level.

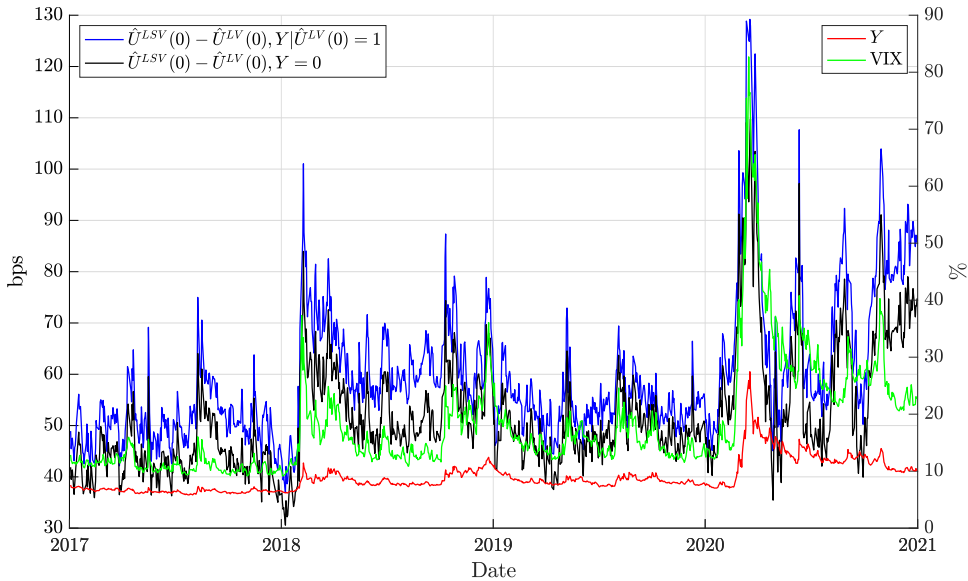


FIGURE 17. Evolution of  $\hat{U}^{LSV}(0) - \hat{U}^{LV}(0)$  over the period January 3, 2017 to December 31, 2020, for the benchmark ABRC. The green and red lines are the VIX and  $Y$  level in percentage, respectively, see right  $y$ -axis. In blue is  $\Delta^{LSV}$  for  $Y$  such that  $U^{LV}(0) = 1$  and in black is  $\Delta^{LSV}$  for  $Y = 0$  in bps, see left  $y$ -axis.

**5. Conclusion.** This paper investigates the main drivers that affect the pricing of autocallable barrier reverse convertibles, structured products that represent a large share of the equity exotic derivatives market. In the theoretical part of the paper, we first address the construction of the implied volatility surface based on the eSSVI parametrization of total implied variance. Then, we motivate our choice of applying the LSV model to price ABRCs. This motivation is given by the limitations of the LV and SV models. On the one hand, the LV model captures the wrong dynamics of the implied volatility smile and thus systematically misprices the forward-smile and the vol-of-vol risk [6]. On the other hand, SV models do not produce enough curvature to match the short-term implied volatility skew. Consequently, both types of models are unsuitable for pricing and risk managing path-dependent derivatives such as autocallables. Since the LSV models succeed in combining the advantages of the LV and SV models while eliminating their limitations, we employ the Heston-like LSV model in our analysis.

The main contribution of this paper is an in-depth empirical analysis of the pricing of single-asset autocallable barrier reverse convertibles in the Heston local-stochastic volatility model. Employing quasi-Monte Carlo experiments, we investigate the sensitivity of the prices of autocallable derivatives referencing major US indices such as the S&P 500 in the Heston LSV model versus the LV model with respect to the derivative structure, model parameters, referenced underlying, and volatility regime. Generally, we find autocallable barrier reverse convertibles to be valued higher in the Heston LSV model compared to the LV model, and hence the price differences to be positive.

The empirical analysis consists of four parts. First, we show that the derivative structure has a profound impact on the valuation differences. For instance, longer U&O barrier observation tenors and higher coupon levels lead to larger price differences. Second, we demonstrate that the valuation differences increase with the volatility-of-variance  $\eta$ , whereas they decrease with the correlation  $\rho$ , the speed of mean reversion  $\kappa$ , and the long-term level of variance  $\theta$  (see Appendix B). Third, we analyze underlying specific characteristics such as the dividend yield and the implied volatility level. We determine that lower forwards reduce the valuation differences, whereas underlyings exhibiting higher implied volatility levels tend to produce larger valuation differences. Finally, we find that the difference between Heston LSV and LV model valuations is positively related to the market's implied volatility level.

There are several directions for future research that this paper leaves open. For instance, our work can be extended by considering underlyings from different asset classes, such as FX, see [10], or multi-underlying autocallables in the spirit of [11], whereby the payoff is written on the “worst-of”. Moreover, we focus on the pricing of autocallables, i.e., the valuation differences at the inception of the trades, and not on the hedging. Hence, we do not study how the valuation differences evolve during the lifetime of the trade as, for example, the underlying level moves towards the barriers with the related risk management implications. Furthermore, more advanced models, such as the two-factor forward variance model from [6], can be considered for driving the stochastic component of LSV models.

Autocallables are the most traded equity-linked exotic derivatives, with yearly volumes amounting to 100 billion euros [40]. Their growth has been exponential since their introduction in 2003 [12]. As a result, the market is well developed, the competition is high, and the margins for autocallables issuers are tightening. In this context and especially for major US indices such as the ones considered in our analysis, price differences of 50 to 100 basis points caused by modeling assumptions that underestimate the costs of autocall vega re-hedging can translate into booking many unprofitable trades for the issuers. Therefore, the results of our work suggest that the correct pricing of autocallables is of utmost importance in consideration of the recent significant losses incurred by leading issuers.

## Appendix A. Theoretical results.

### A.1. Gyöngy's theorem.

**Theorem A.1.** *Let  $Y(t)$  be an Itô process with  $Y(0) = 0$  satisfying*

$$dY(t) = \beta(t, \omega) dt + \delta(t, \omega) dW(t),$$

*where  $\beta(t, \omega)$  and  $\delta(t, \omega)$  are bounded adapted processes such that  $\delta(t, \omega)\delta(t, \omega)^\top$  is uniformly positive definite and  $\omega$  is a sample path of the Brownian motion  $W(t)$ . Then, there exists a Markov process  $Z(t)$  satisfying*

$$dZ(t) = b(t, Z(t)) dt + d(t, Z(t)) dW(t),$$

*with non-random coefficients which admits a weak solution  $Z(t)$  having the same (marginal) distribution as  $Y(t)$  for every  $t$ . Moreover,  $Z(t)$  can be constructed via*

$$b(t, z) = \mathbb{E} [\beta(t, \omega) | Y(t) = z], \quad \text{and} \quad d(t, z)d(t, z)^\top = \mathbb{E} [\delta(t, \omega)\delta(t, \omega)^\top | Y(t) = z].$$

**A.2. Heston LSV model: Discretization.** For the discretization of the instantaneous variance process  $V(t)$ , we rely on the quadratic-exponential (QE) scheme of [3]. For the discretization of the underlying asset price process  $S(t)$ , we follow [44], whose approach is inspired by [3] and outlined below.

By recalling that  $W^S(t)$  is almost surely equal to  $\rho W^V(t) + \sqrt{1 - \rho^2} W(t)^\perp$ , where  $W^V(t)$  and  $W(t)^\perp$  are independent  $\mathbb{Q}$ -Brownian motions, we can rewrite the SDE from Eq. (1) as:

$$\begin{aligned} dS(t) = & (r(t) - q(t))S(t)dt + \rho L(t, S(t))\sqrt{V(t)}S(t)dW^V(t) \\ & + \sqrt{1 - \rho^2}L(t, S(t))\sqrt{V(t)}S(t)dW^\perp(t). \end{aligned} \quad (8)$$

Applying Itô's lemma to  $\log S(t)$ , where the dynamics of  $S(t)$  and  $V(t)$  are given by Eq. (8) and Eq. (2), respectively, we obtain:

$$\begin{aligned} d\log S(t) = & \left( r(t) - q(t) - \frac{1}{2}L^2(t, S(t))V(t) \right) dt + \rho L(t, S(t))\sqrt{V(t)}dW^V(t) \\ & + \sqrt{1 - \rho^2}L(t, S(t))\sqrt{V(t)}dW^\perp(t). \end{aligned}$$

In integral form, we have:

$$\begin{aligned} \log S(t_{j+1}) = & \log S(t_j) + \int_{t_j}^{t_{j+1}} (r(u) - q(u)) du - \frac{1}{2} \int_{t_j}^{t_{j+1}} L^2(u, S(u))V(u)du \\ & + \rho \int_{t_j}^{t_{j+1}} L(u, S(u))\sqrt{V(u)}dW^V(u) \\ & + \sqrt{1 - \rho^2} \int_{t_j}^{t_{j+1}} L(u, S(u))\sqrt{V(u)}dW^\perp(u). \end{aligned}$$

As the effective variance process is also driven by a state-dependent LV component, we perform a local-freezing of  $L(u, S(u))$ , i.e., we use the approximation

$$\int_{t_j}^{t_{j+1}} L(u, S(u))\sqrt{V(u)}dW^V(u) \approx L(t_j, S(t_j)) \int_{t_j}^{t_{j+1}} \sqrt{V(u)}dW^V(u),$$

which leads to

$$\begin{aligned} \log S(t_{j+1}) = & \log S(t_j) + \log \frac{F(0, t_{j+1})}{F(0, t_j)} - \frac{1}{2} \int_{t_j}^{t_{j+1}} L^2(u, S(u))V(u)du \\ & + \frac{\rho}{\eta} L(t_j, S(t_j)) \left( V(t_{j+1}) - V(t_j) - \kappa\theta(t_{j+1} - t_j) + \kappa \int_{t_j}^{t_{j+1}} V(u)du \right) \\ & + \sqrt{1 - \rho^2} \int_{t_j}^{t_{j+1}} L(u, S(u))\sqrt{V(u)}dW^\perp(u). \end{aligned}$$

In the Euler scheme, integrals with respect to time are approximated by

$$\int_{t_j}^{t_{j+1}} a(Y(u))du \approx a(Y(t_j))(t_{j+1} - t_j).$$

Moreover, as  $W(t)^\perp$  is independent of  $V(t)$ , by Itô's isometry, and conditional on  $\int_{t_j}^{t_{j+1}} L^2(u, S(u))V(u)du$  and  $V(t_j)$ , we have:

$$\int_{t_j}^{t_{j+1}} L(u, S(u))\sqrt{V(u)}dW^\perp(u) \sim \mathcal{N} \left( 0, \int_{t_j}^{t_{j+1}} L^2(u, S(u))V(u)d(u) \right).$$

The discretized process  $\log \hat{S}(t)$  finally reads:

$$\begin{aligned} \log \hat{S}(t_{j+1}) &= \log \hat{S}(t_j) + \log \frac{F(0, t_{j+1})}{F(0, t_j)} - \frac{1}{2} \hat{L}^2(t_j, \hat{S}(t_j)) \hat{V}(t_j)(t_{j+1} - t_j) \\ &\quad + \frac{\rho}{\eta} \hat{L}(t_j, \hat{S}(t_j)) (\hat{V}(t_{j+1}) - \hat{V}(t_j) - \kappa \theta(t_{j+1} - t_j) + \kappa \hat{V}(t_j)(t_{j+1} - t_j)) \\ &\quad + \sqrt{1 - \rho^2} \sqrt{\hat{L}^2(t_j, \hat{S}(t_j)) \hat{V}(t_j)} \sqrt{t_{j+1} - t_j} Z_{j+1}^S, \end{aligned} \quad (9)$$

for  $j = 0, \dots, m-1$  and where  $Z_1^S, \dots, Z_m^S$  are i.i.d.  $\mathcal{N}(0, 1)$  variables independent of the discretized process  $\hat{V}(t)$ , which is obtained with the QE scheme, and

$$\hat{L}(t_j, \hat{S}(t_j)) = \frac{\sigma_{LV}(t_j, \hat{S}(t_j))}{\sqrt{\mathbb{E}^Q[V(t_j) | S(t_j) = \hat{S}(t_j)]}}. \quad (10)$$

In the following section, we address the approximation of conditional expectation in Eq. (10) and the derivation of  $\sigma_{LV}$ . It is worth noting that the calibration and simulation of the model can occur simultaneously.

**A.3. Heston LSV model: Calibration.** The LSV model is generally calibrated in two steps [43]. First, the pure stochastic volatility model, i.e., Heston [30] in our implementation, is calibrated to market data. In the second step, the calibration of the leverage function  $L(t, S)$ , which corrects the volatilities implied by the pure SV model towards the volatilities implied by the pure LV model, takes place.

Different approaches have been proposed for the calibration of the leverage function. Our implementation follows closely [44], who propose a novel Monte Carlo technique for the evaluation of the conditional expectation  $\mathbb{E}^Q[V(t) | S(t) = S]$ . Their idea is presented below and is similar to [24].

The approach consists in simulating the Heston LSV model with the discretization scheme in Eq. (9) for  $S(t)$  combined with the QE scheme of [3] for  $V(t)$ . To update the value of  $\hat{S}$  from  $t_j$  to  $t_{j+1}$ , we need to establish the two elements:  $\sigma_{LV}(t_j, S)$  and  $\mathbb{E}[V(t_j) | S(t_j) = S]$ . For the first component, we rely on the formulation of Eq. (5) in terms of log-forward-moneyness  $k := \log K/F(0, T)$  and total implied variance  $w(k, T) := \hat{\sigma}^2(e^k F(0, T), T)$ :

$$\sigma_{LV}^2(e^k F(0, T), T) = \frac{\frac{\partial w}{\partial T}}{1 - \frac{k}{w} \frac{\partial w}{\partial k} + \frac{1}{4} \left( -\frac{1}{4} - \frac{1}{w} + \frac{k^2}{w^2} \right) \left( \frac{\partial w}{\partial k} \right)^2 + \frac{1}{2} \frac{\partial^2 w}{\partial k^2}}.$$

The above equation stems from the fact that implied volatilities are widely used to quote market prices of options. Thus, we can rewrite the option price  $C(K, T)$  as  $C^{BS}(K, T, \hat{\sigma}(K, T))$  and express Eq. (5) in terms of  $\hat{\sigma}(K, T)$  or in our case, but equivalently, in terms of  $w(k, T)$ . The reader is referred to [19] for the proof. We take the same approach to derive the local volatility function for the simulation of the pure LV model.

The expression for  $w$  is given by the eSSVI parametrization of [28]. For any option maturity  $T \geq 0$ , the eSSVI formula describes  $w$  as a function of  $k$  and the ATMF total implied variance  $\theta_T := w(0, T)$ :

$$w(k, \theta_T) = \frac{\theta_T}{2} \left( 1 + \rho(\theta_T) \varphi(\theta_T) k + \sqrt{(\varphi(\theta_T) k + \rho(\theta_T))^2 + 1 - \rho(\theta_T)^2} \right), \quad (11)$$

where  $\varphi : \mathbb{R}_+^* \mapsto \mathbb{R}_+^*$  is a smooth curvature function such that  $\lim_{T \rightarrow 0} \theta_T \varphi(\theta_T)$  exists in  $\mathbb{R}$  and  $\rho(\theta_T) \in (-1, 1)$  controls the rotation of the smile [21]. It is further assumed

that  $\theta$  is a function of  $T$  at least of class  $C^1$  on  $\mathbb{R}_+^*$  and that  $\theta_0 := \lim_{T \rightarrow 0} \theta_T = 0$  because an ATM option with 0 time to maturity has no value [21].

Since eSSVI is an extension of SVI, the implied variance  $\hat{\sigma}^2(e^k F(0, T), T)$  is linear in  $k$  for  $|k| \rightarrow \infty$  and a fixed  $T$  [21]. Hence, it is consistent with the moment formula from [35].

For  $\varphi$ , we rely on the so-called “power-law” representation:

$$\varphi(\theta) = \eta\theta^{-\lambda}, \quad (12)$$

where  $\lambda \in (0, 1)$  and  $\eta > 0$  to ensure positivity, while, for  $\rho$ , [27] finds the following to work well for equity indices:

$$\rho(\theta) = \rho_m + (\rho_0 - \rho_m) \exp\{-a\theta\}, \quad (13)$$

where  $|\rho_0| < 1, |\rho_m| < 1$  and  $a \geq 0$ . The theorems that give the conditions on the parameters in Eqs. (11) to (13) for the eSSVI surface to be free of static arbitrage are presented in [21] and [28].

The second component, namely the evaluation of the conditional expectation, is more complex. The main challenge is the fact that, for each simulated realization of  $S(t)$ , exactly one single corresponding realization of  $V(t)$  is available [44].

Following [44], we use a non-parametric approach enhanced with a continuous approximation. Assume that, for each  $t_j$ ,  $j = 1, \dots, m$ , we have a set of  $n$  Monte Carlo realizations  $\{(\hat{S}_i(t_j), \hat{V}_i(t_j))\}_{i=1}^n$ , simulated according to the scheme of Eq. (9) and the quadratic-exponential scheme, respectively, for which we need to evaluate the conditional expectation in Eq. (10).

To overcome the fact that for each  $\hat{S}_i(t_j)$  we dispose of exactly one value of  $\hat{V}_i(t_j)$ , and hence the expectation conditional on  $\hat{S}_i(t_j)$  is equal to  $\hat{V}_i(t_j)$ , we partition  $\hat{S}(t_j)$  into  $\ell$  mutually exclusive bins, whereby each bin is defined to contain nearly the same number of paths [44]. Define by  $\{(\bar{S}_i(t_j), \bar{V}_i(t_j))\}_{i=1}^n$  the set of ordered realizations such that  $\bar{S}_1(t_j) \leq \dots \leq \bar{S}_n(t_j)$ , the set of bins is then given by:

$$\mathcal{B} = \{(b_k, b_{k+1}]\}_{k=1}^\ell,$$

where  $b_1 = \bar{S}_1(t_j)$ ,  $b_{\ell+1} = \bar{S}_n(t_j)$ , and  $b_k = \bar{S}_{(k-1)n/\ell}(t_j)$ , for  $k = 2, \dots, \ell$ . Note that the set of bins  $\mathcal{B}$  is dependent on the time step  $t_j$ . For a specific realization  $S \in (b_k, b_{k+1}]$ , [44] show that the following approximation is justified and appropriate:

$$\begin{aligned} \mathbb{E}^Q[V(t_j) | S(t_j) = S] &\approx \frac{\mathbb{E}^Q[V(t_j) \mathbf{1}_{S(t_i) \in (b_k, b_{k+1})}]}{\mathbb{Q}(S(t_i) \in (b_k, b_{k+1}))} \\ &\approx \frac{\frac{1}{n} \sum_{i=1}^n \hat{V}_i(t_j) \mathbf{1}_{S \in (b_k, b_{k+1})}}{\mathbb{Q}(\hat{S}(t_i) \in (b_k, b_{k+1}))} \\ &= \frac{\ell}{n} \sum_{i \in \mathcal{I}_k} \hat{V}_i(t_j), \end{aligned} \quad (14)$$

where  $\mathcal{I}_k$  denotes the set of path numbers corresponding to the  $k$ -th bin  $B_k$ , i.e.,  $\mathcal{I}_k = \{i \mid (\hat{S}_i(t_j), \hat{V}_i(t_j)) \in B_k\}$ , and  $\mathbf{1}$  is the indicator function.

With Eq. (14), the conditional expectation is approximated by means of a step-function. The continuous approximation (CA) consists of connecting the mid points of the approximations obtained with the non-parametric method described above [44]. In contrast to the simple method, the CA is continuous and provides a greater fit to the theoretical conditional expectation, see Fig. 18. For an increasing number

of simulations  $n$  and bins  $\ell$ , the approximation recovered by the non-parametric method converges to the theoretical value [44].

Figure 18 allows us to graphically visualize the functioning of the non-parametric method and the quality of the approximations for the Heston model. Figure 19

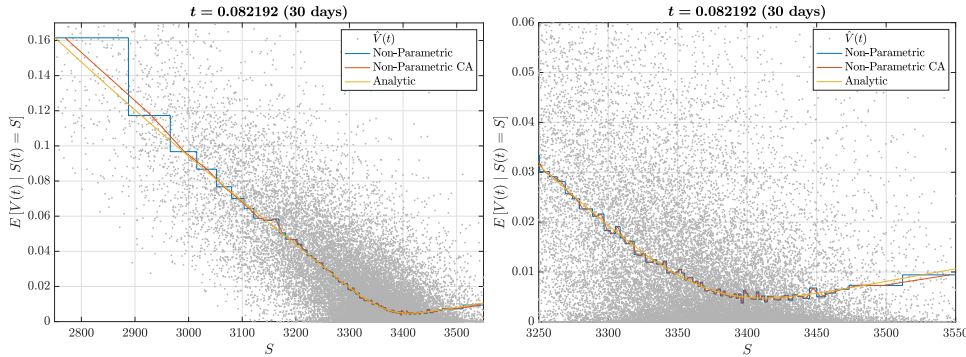


FIGURE 18. Approximation of the conditional expectation  $\mathbb{E}^{\mathbb{Q}}[V(t) | S(t) = S]$ , where the joint dynamics of  $(S(t), V(t))_{t \geq 0}$  is given by the Heston model with  $\kappa = 3.7764$ ,  $\theta = 0.0365$ ,  $\eta = 0.9555$ ,  $\rho = -0.7946$ , and  $V_0 = 0.0141$ .  $T_{max} = 1057$  days,  $\ell = 100$ ,  $n = 2^{14}$ , and  $m = 1057$ .

illustrates the non-parametric approximation of the conditional expectation for the Heston LSV model. For the latter, we cannot show a comparison with the theoretical value as this is not available analytically. Here,  $T_{max}$  corresponds to the longest listed SPX expiry as of January 23, 2020.

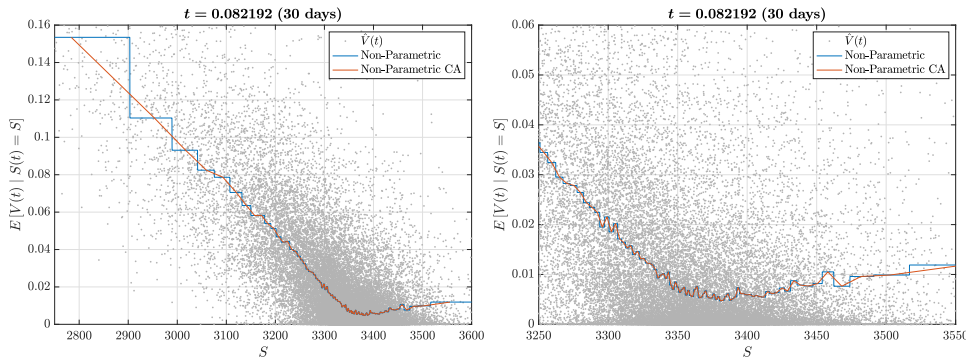


FIGURE 19. Approximation of the conditional expectation  $\mathbb{E}^{\mathbb{Q}}[V(t) | S(t) = S]$ , where the joint dynamics of  $(S(t), V(t))_{t \geq 0}$  is given by the system of SDEs from Eqs. (1) to (3). The LV function is obtained as of January 23, 2020,  $T_{max} = 1057$  days,  $\ell = 100$ ,  $n = 2^{14}$ , and  $m = 1057$ . The Heston parameters are as in Fig. 18.

Figure 20 exhibits the approximate leverage function  $\hat{L}(t, S)$  calibrated to SPX options as of January 23, 2020. We observe that the local volatility correction lies in the interval  $[0.5, 1.5]$  and that its values close to ATMF are around 1. This is in

accordance with [29], who claims that, in order to maintain the dynamic properties of the underlying SV model, the value of  $L(t, S)$  around ATMF should be close to 1 and its skew not too remarkable.

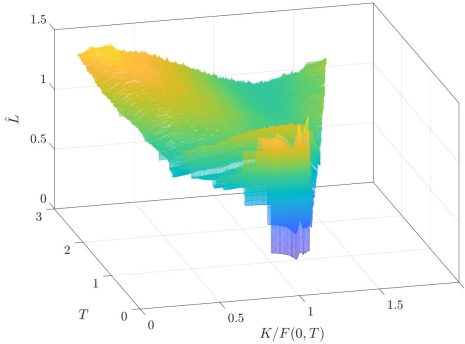


FIGURE 20. Leverage function approximation calibrated to SPX options as of January 23, 2020. The parameters for the approximation are  $T_{max} = 1057$  days,  $\ell = 200$ ,  $n = 2^{18}$ , and  $m = 1057$ .

The fact that the leverage function approximation is not smooth is due to the non-parametric approximation method and depends on the choice of the number of bins  $\ell$  as well as the number of MC paths  $n$ . Yet, this does not have a significant impact on prices. Also, observe in Fig. 20 that the non-parametric method does not allow recovering an approximation for the conditional expectation in low probability density areas, i.e., for  $K \rightarrow 0$  or  $K \rightarrow \infty$ , and especially for  $T \rightarrow 0$ .

## Appendix B. Empirical results.

**B.1. Autocallables pricing: Structure sensitivity.** To investigate the impact of the autocall coupon, we set  $Y = 0$  and solve for  $\mathbf{Y}^{AC}$  such that  $U^{LV}(0) = 1$  for each  $T^E$ . The results are presented in Table 4. For each period  $i = 1, \dots, N$ , we define the autocall coupon  $\mathbf{Y}^{AC}$  to be “snowballing”, i.e.,  $Y_i^{AC} = i \frac{T^O}{12} \bar{Y}^{AC}$ .

$T^E$	3	6	9	12	15	18	21	24	30	36	42
$\bar{Y}^{AC}$	6.24%	9.03%	10.39%	10.96%	11.06%	11.24%	11.23%	11.13%	11.00%	10.8%	10.67%
$T^E$	48	54	60	66	72	78	84	90	96	108	120
$\bar{Y}^{AC}$	10.37%	10.15%	10.13%	9.92%	9.74%	9.69%	9.52%	9.37%	9.17%	8.99%	8.96%

TABLE 4.  $\bar{Y}^{AC}$  for different  $T^E$ , computed as of January 23, 2020.

Similarly to Fig. 8a, Fig. 21a shows that the Heston LSV model leads to higher prices compared to LV, whereby the difference  $\Delta^{LSV}$  is generally larger the longer the observation tenor  $T^O$ . However, for  $T^O = 6$  and 12, we note that  $\Delta^{LSV}$  increases almost linearly with  $T^E$ . Moreover, in contrast to Fig. 8a, the price differences are smaller for short expiry tenors and vice versa for longer expiry tenors. For  $T^O = 1$  and 3,  $\Delta^{LSV}$  is smaller compared to the base case for all  $T^E$ . To summarize, our observation implies that, for long  $T^O$  and for  $T^E > 72$ , the autocall coupon implies a larger model-dependency compared to the standard coupon case, while the reverse situation applies for  $T^E \leq 72$ .

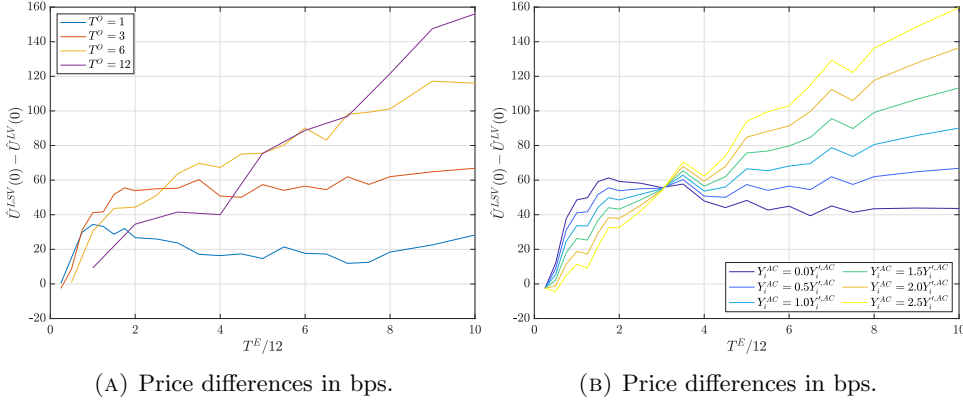


FIGURE 21.  $\hat{U}^{LSV}(0) - \hat{U}^{LV}(0)$  for different observation tenors  $T^O$  and autocall coupon levels  $\mathbf{Y}^{\mathbf{AC}}$  across various expiry tenors  $T^E$ .

Figure 21b exhibits that, for a fixed  $T^E$ ,  $\Delta^{LSV}$  scales linearly with  $\mathbf{Y}^{\mathbf{AC}}$ . However, in the time dimension, we observe an inflection point at around the 3 years expiry tenor. For  $T^E < 36$ ,  $\Delta^{LSV}$  decreases with increasing  $\mathbf{Y}^{\mathbf{AC}}$ , while, for  $T^E > 36$ , we observe that  $\Delta^{LSV}$  increases with  $\mathbf{Y}^{\mathbf{AC}}$ .

To analyze the impact of the autocall barrier level, we assume again the base case outlined in Section 4.1. Figure 22 displays the price differences between Heston LSV and LV for several constant autocall barrier levels.

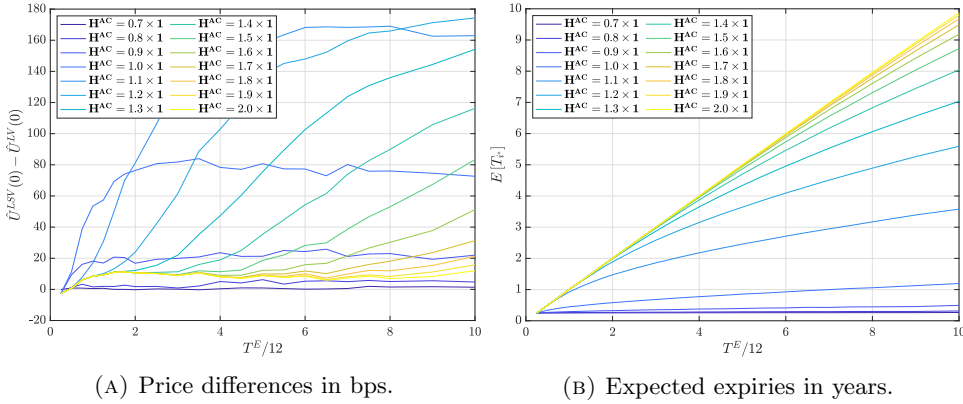


FIGURE 22. In the left panel,  $\hat{U}^{LSV}(0) - \hat{U}^{LV}(0)$  for different constant autocall barrier levels  $\mathbf{H}^{\mathbf{AC}}$  and across different  $T^E$ . In the right panel, the LV implied  $\mathbb{E}^Q[T_{i^*}]$ .

We observe that, for low barrier levels, the high probability of early redemption translates into short expected expiries and minor  $\Delta^{LSV}$ . Essentially, if  $\mathbf{H}^{\mathbf{AC}}$  is low, the autocallable derivative becomes a short fixed maturity structure.

We observe the same for high  $\mathbf{H}^{\mathbf{AC}}$ . Thereby, low probabilities of breaching the autocall barriers essentially induce fixed maturity into the structure and reduce its path-dependency. As a consequence, the Heston LSV and LV prices agree, up to a pricing error induced by different discretization schemes. This leads, for a fixed

expiry tenor  $T^E$ , to a concave dependency between  $\mathbf{H}^{\mathbf{AC}}$  and  $\Delta^{LSV}$ , where the structures whose autocall barrier levels imply  $\mathbb{E}^{\mathbb{Q}}[T_{i^*}] \approx \frac{1}{2}T^E$  exhibit larger price differences. For a 6 years ABRC with  $\mathbf{H}^{\mathbf{AC}} = 1.1 \times \mathbf{1}$ , the price difference implied by our models is as high as 1.70%.

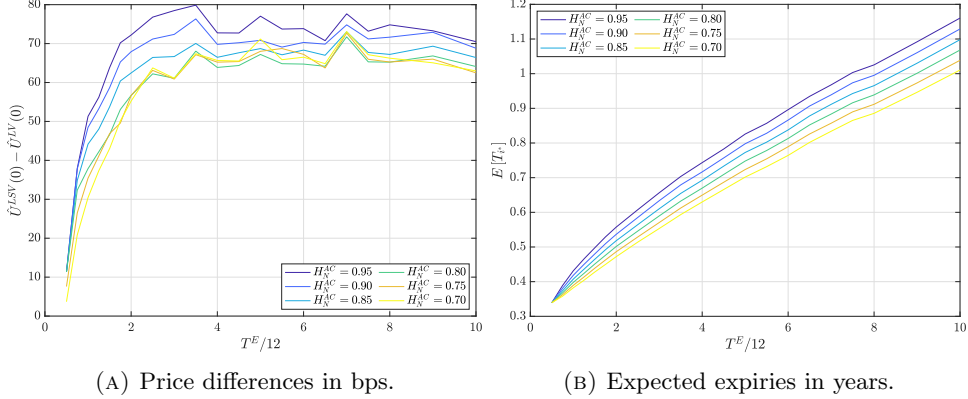


FIGURE 23. In the left panel,  $\hat{U}^{LSV}(0) - \hat{U}^{LV}(0)$  for different step-down autocall barrier levels  $\mathbf{H}^{\mathbf{AC}}$  and across different  $T^E$ ,  $H_1^{\mathbf{AC}} = 1$ . In the right panel, the LV implied  $\mathbb{E}^{\mathbb{Q}}[T_{i^*}]$ .

A popular feature of ABRCs known as “step-down” generally refers to linearly decreasing autocall barrier levels. Consider, for instance,  $T^E = 18$  and  $T^O = 3$ , then, if  $H_1^{\mathbf{AC}} = 1$  and  $H_N^{\mathbf{AC}} = 0.95$ , we have  $H_i^{\mathbf{AC}} = H_1^{\mathbf{AC}} + \frac{i-1}{N-1}(H_1^{\mathbf{AC}} - H_N^{\mathbf{AC}})$ , for  $i = 2, \dots, N-1$ , i.e.,  $\mathbf{H}^{\mathbf{AC}} = (1.00, 0.99, 0.98, 0.97, 0.96, 0.95)$ . The step-down feature reduces the impact of LSV by reducing significantly the expected expiry  $\mathbb{E}^{\mathbb{Q}}[T_{i^*}]$ , as shown in Fig. 23. The lower the last barrier level  $H_N^{\mathbf{AC}}$  is, the smaller the model valuation differences  $\Delta^{LSV}$  are.

**B.2. Autocallables pricing: Parameter sensitivity.** Observing Fig. 11, the magnitude of the effect of an increase in  $\eta$  is roughly constant across expiry tenors for  $T^E \geq 36$ . However, for autocall barrier levels that lead to a longer expected time to expiry, such as in Fig. 22, we expect this to increase with  $T^E$ .

In fact, our claim is confirmed by Fig. 24, which exhibits  $\Delta^{LSV}$  across different expiry tenors  $T^E$  and volatility of variance levels  $\eta$  for the benchmark ABRC with higher autocall barriers, i.e.,  $\mathbf{H}^{\mathbf{AC}} = 1.2 \times \mathbf{1}$ .

We observe in Fig. 25 the sensitivity of the ABRC’s price with respect to the speed of mean reversion. Thereby,  $\Delta^{LSV}$  is inversely related to  $\kappa$ . The effect is nearly constant across  $T^E$  for the basic ABRC.

Similarly to  $\eta$ , although in opposite direction, the effect of  $\kappa$  on  $\Delta^{LSV}$  becomes increasingly smaller for larger values of  $\kappa$ . Furthermore, the autocall probability increases with  $\kappa$ , leading to a shorter expected time to expiry. Inspection of the forward-starting IV smile provides insights for our observation.

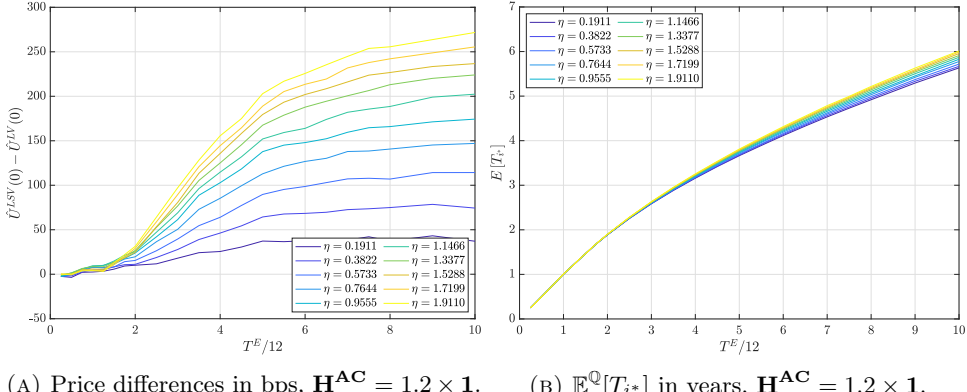


FIGURE 24.  $\hat{U}^{LSV}(0) - \hat{U}^{LV}(0)$  for different volatility of variance levels  $\eta$  across various expiry tenors  $T^E$ . In the right panel, the corresponding Heston LSV expected expiries  $E^{\mathbb{Q}}[T_{i^*}]$ .

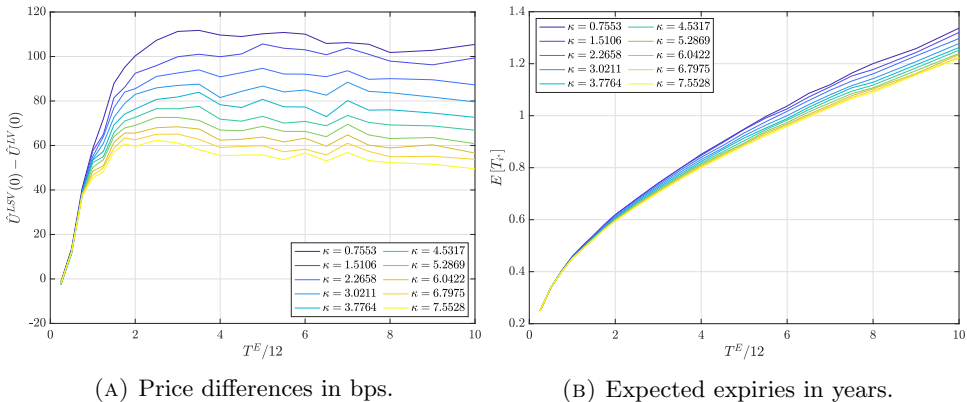


FIGURE 25.  $\hat{U}^{LSV}(0) - \hat{U}^{LV}(0)$  for different speed of mean reversion levels  $\kappa$  across various expiry tenors  $T^E$ . In the right panel, the corresponding LSV expected expiries  $E^{\mathbb{Q}}[T_{i^*}]$ .

As shown in Fig. 26a, the forward ATM skew decreases with increasing  $\kappa$ . In turn, this leads to lower future vol-of-vol levels and higher forward ATM IVs. Hence, the ABRC's prices are driven lower, implying reduced differences between the Heston LSV and LV models. Intuitively, large values of  $\kappa$  imply that the volatility becomes “less stochastic” as any shock in the volatility process is rapidly tamed by the high speed of mean reversion.

For the long-term variance level, we expect the Heston LSV price of the ABRC to decrease with  $\theta$ . Indeed, larger  $\theta$  means higher long-term volatility levels, and

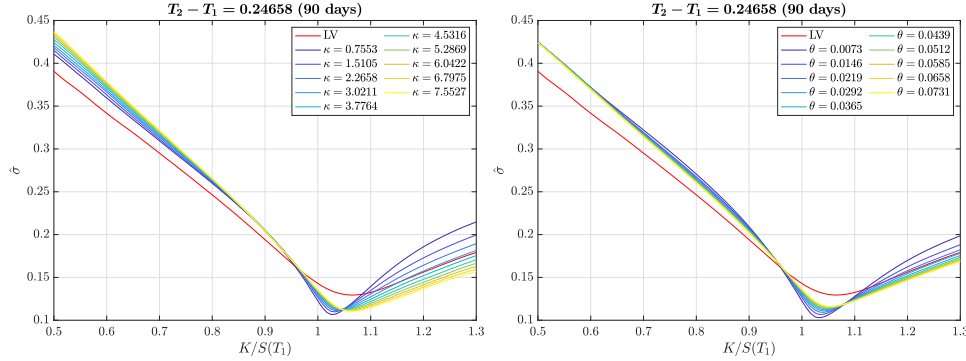
(A) 90-days Forward IV smile for different  $\kappa$ . (B) 90-days Forward IV smile for different  $\theta$ .

FIGURE 26.  $T_1 = 3$  months forward-starting IV smiles generated by the Heston-like LSV model calibrated to SPX option as of January 23, 2020, for different levels of  $\kappa$  and  $\theta$ .

the ABRC's vega is negative, see Fig. 7a. Our claim is supported by the observation of Fig. 27. Observe that  $\Delta^{LSV}$  is inversely related to  $\theta$ . The relationship is not linear but rather concave, as already observed for  $\eta$  and  $\kappa$ . In addition,  $\mathbb{E}^{\mathbb{Q}}[T_{i^*}]$  decreases with  $\theta$ . The influence of Heston's  $\theta$  parameter is explained by the forward IV smile in Fig. 26b. With higher  $\theta$ , the forward ATM skew flattens, while the forward ATM IVs increase.

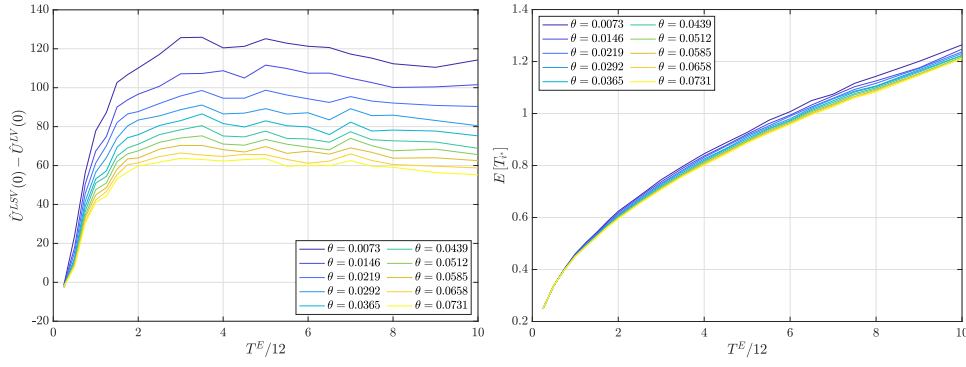


FIGURE 27.  $\hat{U}^{LSV}(0) - \hat{U}^{LV}(0)$  for different long-term variance levels  $\theta$  across various expiry tenors  $T^E$ . In the right panel, the corresponding LV expected expiries  $\mathbb{E}^{\mathbb{Q}}[T_{i^*}]$ .

The initial level of variance  $V_0$  has negligible influence on the valuation differences of the ABRC between the two models and hence no result is presented.

**B.3. Autocallables pricing: Underlying sensitivity.** Table 5 and Table 6 exhibit the eSSVI and Heston parameters calibrated to SPX, NDX, DDX, and RUT options as of January 23, 2020, respectively. The eSSVI parameters are very close among the four indices. The main difference lies in the vector parameter  $\theta$ , which denotes the AMTF term structure of total implied variance, displayed in the right panel of Fig. 28.

	$\eta$	$\lambda$	$\rho_m$	$\rho_0$	$a$
SPX	0.6066	0.5929	-0.7564	-0.4245	651.0968
NDX	0.5692	0.5741	-0.7593	-0.3328	724.3588
DDX	0.5752	0.5771	-0.7715	-0.4323	200.0267
RUT	0.5706	0.5971	-0.6823	-0.3437	387.2297

TABLE 5. eSSVI parameters calibrated to SPX, NDX, DDX, and RUT traditional, weekly, and end-of-month options as of January 23, 2020.

The AMTF implied volatilities of SPX and DDX essentially agree, while RUT and NDX exhibit around 2% and 3% higher IV levels, respectively. On the other hand, Heston parameters are further apart, although the values of  $\theta$  and  $V_0$  reflect what is mentioned above about the ATMF implied volatility term structures.

	$\kappa$	$\theta$	$\eta$	$\rho$	$V_0$
SPX	3.7764	0.0365	0.9555	-0.7946	0.0141
NDX	3.5723	0.0463	0.8791	-0.7784	0.0242
DDX	2.0432	0.0388	0.5728	-0.7919	0.0159
RUT	4.6137	0.0409	1.0805	-0.7206	0.0205

TABLE 6. Heston parameters calibrated to SPX, NDX, DDX, and RUT traditional options as of January 23, 2020.

The left panel of Fig. 28 displays the forwards in percentage of the spot, i.e.,  $F(0, T)/S(0)$ , for different tenors  $T$ . The constituents of DDX and SPX are paying higher dividends compared to those of RUT and NDX as reflected by their forward curves. Implied dividend yields inclusive of borrow rates for the longest maturity are 2.08%, 1.64%, 1.15%, and 0.78%, respectively.

**B.4. Autocallables pricing: Market sensitivity.** Table 7 outlines the underlying information that defines four volatility regimes as proxied by the VIX: low as of November 3, 2017, medium-low as of June 23, 2020, medium-high as of March 31, 2020, and high as of March 17, 2020.

Figures 29a and 29c depict  $\Delta^{LSV}$  for the benchmark structure with the coupon  $Y$  defined such that  $U^{LV}(0) = 1$ , whereas Figs. 29b and 29d show the results for

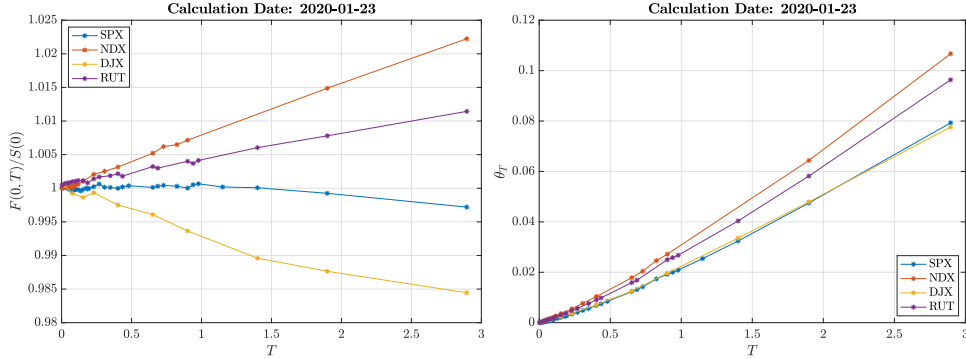


FIGURE 28. SPX, NDX, DJX, and RUT ATM total implied variance and forwards term structure as of January 23, 2020.

$Y = 0$ , hence isolating the impact of  $Y$  on  $\Delta^{LSV}$ . Medium-low and medium-high volatility regimes are presented here. An interested reader can compare the results to Fig. 16.

Table 8 exhibits the eSSVI and Heston parameters calibrated to options data as of the four scenario dates from Section 4.5. Observe that, in stressed markets, the calibration of the Heston model tends to produce large values of  $\eta$ ,  $\kappa$ ,  $V_0$ , and  $\theta$  as well as low spot-variance correlations  $\rho$ . Even though, as shown in Appendix B.2, high  $\theta$  and  $\kappa$  tend to reduce  $\Delta^{LSV}$ , the effect of high  $\eta$  and low  $\rho$  appears to be prevailing. Indeed,  $\Delta^{LSV}$  increases with the volatility level of the underlying, as shown in Figs. 16 and 29.

	VIX	$\sigma(F(0,T), T)$					$F(0,T)/S(0)$					
		T	1/4	1/2	1	2	3	1/4	1/2	1	2	3
2017-11-08	SPX	9.14	0.0923	0.1098	0.1309	0.1525	0.1628	0.9995	0.9993	0.9990	1.0013	1.0052
	NDX		0.1350	0.1497	0.1647	0.1755	0.1905	1.0008	1.0028	1.0072	1.0188	1.0317
	DJX		0.1009	0.1167	0.1325	0.1436	0.1485	0.9971	0.9957	0.9955	0.9936	0.9933
	RUT		0.1397	0.1541	0.1708	0.1827	0.1911	1.0001	1.0006	1.0017	1.0057	1.0118
2020-06-23	SPX	31.37	0.2652	0.2717	0.2545	0.2381	0.2298	0.9969	0.9938	0.9876	0.9754	0.9640
	NDX		0.2809	0.2848	0.2666	0.2536	0.2485	0.9995	0.9984	0.9967	0.9924	0.9887
	DJX		0.2945	0.2914	0.2632	0.2434	0.2378	0.9955	0.9911	0.9839	0.9709	0.9564
	RUT		0.3575	0.3445	0.3009	0.2691	0.2543	0.9982	0.9966	0.9940	0.9878	0.9848
2020-03-31	SPX	53.54	0.3920	0.3469	0.2974	0.2554	0.2331	0.9942	0.9933	0.9945	0.9853	0.9784
	NDX		0.3948	0.3388	0.2921	0.2579	0.2415	0.9969	0.9969	0.9976	1.0003	1.0002
	DJX		0.4571	0.3874	0.3301	0.2938	0.2631	0.9919	0.9892	0.9805	0.9595	0.9464
	RUT		0.4430	0.3849	0.3273	0.2849	0.2650	0.9909	0.9890	0.9858	0.9837	0.9840
2020-03-17	SPX	75.91	0.5872	0.4779	0.3763	0.2944	0.2875	0.9861	0.9815	0.9771	0.9690	0.9600
	NDX		0.5776	0.4679	0.3682	0.3000	0.2696	0.9902	0.9886	0.9835	0.9774	0.9741
	DJX		0.6313	0.5026	0.3960	0.3357	0.3340	0.9832	0.9769	0.9659	0.9441	0.9278
	RUT		0.5941	0.4874	0.3834	0.3195	0.2931	0.9817	0.9786	0.9716	0.9591	0.9483

TABLE 7. VIX levels, ATM total implied volatilities, and forwards versus different tenors  $T$  as of November 3, 2017, June 23, 2020, March 31, 2020, and March 17, 2020, respectively.

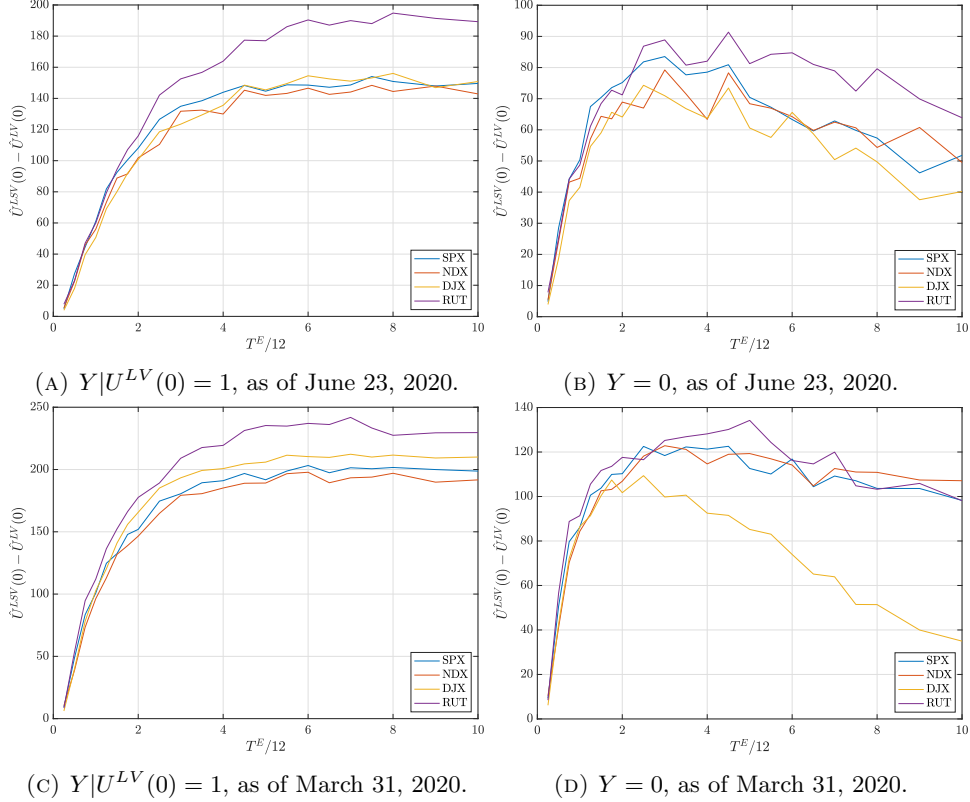


FIGURE 29.  $\hat{U}^{LSV}(0) - \hat{U}^{LV}(0)$  for SPX, NDX, DJX, and RUT across expiry tenors  $T^E$ , in medium-low and medium-high volatility regimes and for different coupon amounts  $Y$ .

		eSSVI					Heston				
		$\eta$	$\lambda$	$\rho_m$	$\rho_0$	$a$	$\kappa$	$\theta$	$\eta$	$\rho$	$V_0$
2017-11-03	SPX	0.7303	0.5981	-0.7126	-0.3635	676.32	2.8555	0.0401	1.0806	-0.7473	0.0046
	NDX	0.6122	0.5816	-0.6759	-0.1902	513.85	4.4025	0.0428	1.0791	-0.6989	0.0135
	DJX	0.6499	0.6135	-0.6243	-0.0435	589.12	3.9711	0.0325	1.0894	-0.6900	0.0052
	RUT	0.6504	0.5918	-0.6141	-0.2397	364.16	4.3905	0.0464	1.2418	-0.6534	0.0173
2020-06-23	SPX	0.9664	0.4963	-0.7633	-0.2269	340.68	2.0230	0.0964	1.3275	-0.8176	0.1052
	NDX	0.9439	0.4900	-0.6838	-0.2543	306.51	1.7808	0.1040	1.2268	-0.7328	0.1126
	DJX	0.7798	0.5500	-0.7816	-0.3627	83.62	1.7819	0.0860	1.1351	-0.8111	0.1284
	RUT	1.1080	0.4078	-0.7628	-0.3608	120.76	1.7505	0.1032	1.3331	-0.7843	0.1911
2020-03-31	SPX	0.7710	0.5231	-0.8321	-0.4816	137.92	4.6048	0.0805	2.2566	-0.8245	0.3137
	NDX	0.7687	0.5227	-0.7706	-0.2908	212.56	4.2299	0.0766	2.0220	-0.7809	0.2971
	DJX	1.1234	0.4049	-0.6938	-0.5099	4854.88	3.8431	0.0882	2.1734	-0.7513	0.4058
	RUT	1.1092	0.4148	-0.7463	-0.4252	125.98	4.6056	0.1118	2.8350	-0.7620	0.4234
2020-03-17	SPX	1.1246	0.3460	-0.9227	-0.6585	120.92	6.0662	0.0940	3.4464	-0.8911	0.8440
	NDX	0.6885	0.4514	-0.9641	-0.9273	3841.28	6.4882	0.0780	2.4367	-0.8998	0.7813
	DJX	1.2104	0.2882	-0.8558	-0.8092	1449.55	5.8442	0.0938	3.7716	-0.8190	1.0221
	RUT	0.9665	0.3153	-0.9951	-0.9929	1449.54	5.5594	0.1057	2.6639	-0.9176	0.7730

TABLE 8. eSSVI and Heston parameters calibrated to options data in different volatility regimes for SPX, NDX, DJX, and RUT.

**Acknowledgments.** To the memory of Peter Carr.

## REFERENCES

- [1] Y. Aït-Sahalia and A. W. Lo, Nonparametric estimation of state-price densities implicit in financial asset prices, *The Journal of Finance*, **53** (1998), 499-547.
- [2] T. Alm, B. Harrach, D. Harrach and M. Keller, [A monte Carlo pricing algorithm for autocallables that allows for stable differentiation](#), *Journal of Computational Finance*, **17** (2013), 43-70.
- [3] L. Andersen, Simple and efficient simulation of the Heston stochastic volatility model, *Journal of Computational Finance*, **11** (2008), 1-42.
- [4] H. Bartholomew, SocGen mulls sale of structured product books after big losses, *Risk.net*, Retrieved from <https://www.risk.net/derivatives/7663541/socgen-mulls-sale-of-structured-product-books-after-big-losses>, 2020.
- [5] H. Bartholomew, N. Somasundaram and L. Becker, Natixis's 260m hit blamed on big books and KospI3 product, *Risk.net*, Retrieved from <https://www.risk.net/derivatives/6229806/natixiss-eu260m-hit-linked-to-rapid-asia-expansion-and-kospI3-leverage>, 2018.
- [6] L. Bergomi, *Stochastic Volatility Modeling*, Boca Raton: CRC Press, 1st edition, 2016.
- [7] F. Black and M. Scholes, [The pricing of options and corporate liabilities](#), *The Journal of Political Economy*, **81** (1973), 637-654.
- [8] M. Bouzoubaa and A. Osseiran, *Exotic Options and Hybrids: A Guide to Structuring, Pricing and Trading*, Hoboken: John Wiley & Sons, 1st edition, 2010.
- [9] I. J. Clark, *Foreign Exchange Option Pricing: A Practitioner's Guide*, Chichester: John Wiley & Sons, 1st edition, 2011.
- [10] A. Cozma, M. Mariapragassam and C. Reisinger, [Convergence of an Euler scheme for a hybrid stochastic-local volatility model with stochastic rates in foreign exchange markets](#), *SIAM Journal on Financial Mathematics*, **9** (2018), 127-170.
- [11] A. De Col and P. Kuppinger, The interplay between stochastic volatility and correlations in equity autocallables, Available at SSRN, 2017.
- [12] G. Deng, J. Mallett and C. McCann, [Modeling autocallable structured products](#), *Journal of Derivatives and Hedge Funds*, **17** (2016), 323-344.
- [13] E. Derman and I. Kani, Riding on a smile, *Risk*, **7** (1994), 32-39.
- [14] B. Dumas, J. Fleming and R. E. Whaley, [Implied volatility functions: Empirical tests](#), *The Journal of Finance*, **53** (1998), 2059-2106.
- [15] B. Dupire, Pricing with a smile, *Risk*, **7** (1994), 18-20.

- [16] M. R. Fengler, Arbitrage-free smoothing of the implied volatility surface, *Quantitative Finance*, **9** (2009), 417-428.
- [17] M. R. Fengler, Option data and modeling BSM implied volatility, In J.-C. Duan, W. K. Härdle, and James E. Gentle, editors, *Handbook of Computational Finance*. Berlin: Springer, 1st edition, 2012, 117-142.
- [18] C. P. Fries and M. S. Joshi, Perturbation stable conditional analytic Monte-Carlo pricing scheme for autocallable products, *International Journal of Theoretical and Applied Finance*, **14** (2011), 197-219.
- [19] J. Gatheral, *The Volatility Surface: A Practitioner's Guide*, Hoboken: John Wiley & Sons, 1st edition, 2006.
- [20] J. Gatheral and A. Jacquier, Convergence of Heston to SVI, *Quantitative Finance*, **11** (2011), 1129-1132.
- [21] J. Gatheral and A. Jacquier, Arbitrage-free SVI volatility surfaces, *Quantitative Finance*, **14** (2014), 59-71.
- [22] P. Glasserman, *Monte Carlo Methods in Financial Engineering*, New York: Springer, 2004.
- [23] T. Guillaume, Autocallable structured products, *The Journal of Derivatives*, **22** (2015), 73-94.
- [24] J. Guyon and P. Henry-Labordére, Being particular about calibration, *Risk*, **25** (2012), 88-93.
- [25] I. Gyöngy, Mimicking the one-dimensional marginal distributions of processes having an ito differential, *Probability Theory and Related Fields*, **71** (1986), 501-516.
- [26] P. Hagan, D. Kumar, A. Lesniewski and D. Woodward, Managing smile risk, *The Best of Wilmott*, **1** (2002), 249-296.
- [27] S. Hendricks, Extending the SSVI model with arbitrage-free conditions, Master's thesis, Delft University of Technology, 2016.
- [28] S. Hendriks and C. Martini, The extended SSVI volatility surface, *Journal of Computational Finance*, **22** (2019), 25-39.
- [29] P. Henry-Labordére, Calibration of local stochastic volatility models to market smiles: A Monte-Carlo approach, *Risk Magazine*, September, (2009), 112-117.
- [30] S. L. Heston, A closed-form solution for options with stochastic volatility with applications to bond and currency options, *The Review of Financial Studies*, **6** (1993), 327-343.
- [31] C. Homescu, Local stochastic volatility models: Calibration and pricing, Available at SSRN, 2014.
- [32] M. Jex, R. Henderson and D. Wang, Pricing exotics under the smile, *Risk*, **12** (1999), 72-75.
- [33] N. Kahalé, An arbitrage-free interpolation of volatilities, *Risk*, **17** (2004), 102-106.
- [34] K.-K. Kim and D.-Y. Lim, A recursive method for static replication of autocallable structured products, *Quantitative Finance*, **19** (2019), 647-661.
- [35] R. W. Lee, The moment formula for implied volatility at extreme strikes, *Mathematical Finance*, **14** (2004), 469-480.
- [36] OptionMetrics, *IvyDB US File and Data Reference Manual*, Retrieved from [https://wrds-www.wharton.upenn.edu/documents/1504/IvyDB\\_US\\_Reference\\_Manual\\_rn2hAXz.pdf](https://wrds-www.wharton.upenn.edu/documents/1504/IvyDB_US_Reference_Manual_rn2hAXz.pdf), 2021.
- [37] V. Piterbarg, Markovian projection method for volatility calibration, Available at SSRN, 2006.
- [38] R. Rebonato, *Volatility and Correlation: The Perfect Hedger and the Fox*, Hoboken: John Wiley & Sons, 2nd edition, 2004.
- [39] Y. Ren, D. Madan and M. Q. Qian, Calibrating and pricing with embedded local volatility models, *Risk*, **20** (2007), 138-143.
- [40] G. Salon, Equity autocalls and vanna negative carries: Pricing and hedging with a simple add-on, Available at SSRN, 2019.
- [41] A. Sepp, Efficient numerical PDE methods to solve calibration and pricing problems in local stochastic volatility models, *Global Derivatives Trading & Risk Management*, 2011.
- [42] N. Sherif, Calling out autocallable pricing, *Risk. Net*, Retrieved from <https://www.risk.net/our-take/6348336/calling-out-autocallable-pricing>, 2019.
- [43] Y. Tian, Z. Zhu, G. Lee, F. Klebaner and K. Hamza, Calibrating and pricing with a stochastic-local volatility model, *The Journal of Derivatives*, **22** (2015), 21-39.
- [44] A. W. van der Stoep, L. A. Grzelak and C. W. Oosterlee, The Heston stochastic-local volatility model: Efficient Monte Carlo simulation, *International Journal of Theoretical and Applied Finance*, **17** (2014), 1450045, 30 pp.

- [45] A. W. van der Stoep, L. A. Grzelak and C. W. Oosterlee, [A novel Monte Carlo approach to hybrid local volatility models](#), *Quantitative Finance*, **17** (2017), 1347-1366.

Received for publication September 2022; early access December 2022.